

Fabrication of a Polysaccharide-Protein/Protein Complex Stabilized Oral Nanoemulsion to Facilitate the Therapeutic Effects of 1,8-Cineole on Atherosclerosis

Yi Chen,[¶] Jianing Wang,[¶] Jinzhan Xu,[¶] Jiyuan Zhang, Shan Xu, Qing Zhang, Jing Huang, Jianqing Peng, Haiyu Xu,^{*} Qianming Du,^{*} and Zipeng Gong^{*}



Cite This: *ACS Nano* 2023, 17, 9090–9109



Read Online

ACCESS |

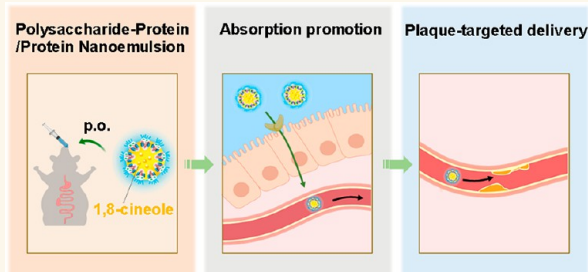
Metrics & More

Article Recommendations

Supporting Information

ABSTRACT: Atherosclerosis (AS) is a systemic disease characterized by lipid deposition in the blood vessel wall that urgently requires effective and safe therapeutic drugs for long-term treatment. An essential oil monomer-1,8-cineole (CIN) with ameliorative effects on vascular injuries has considerable potential for preventing the progression of AS because of its antioxidant, anti-inflammation, and cholesterol regulatory effects. However, the high volatility and instability of CIN result in low oral bioavailability and a short half-life, thereby limiting its clinical application. We formulated a nanoemulsion using a polysaccharide-protein/protein complex (dextran-bovine serum albumin/Active Ingredient, DEX_{sk}-BSA/PTM) as a stabilizer, with vitamin B12 (VB₁₂) as the ligand to facilitate the transportation across the small intestine. An emulsion preparation method using a microjet followed by ultraviolet irradiation was developed to obtain the CIN-loaded oral nanoemulsion CIN@DEX_{sk}-BSA/PTM/VB₁₂. The nanoemulsion improved the stability of CIN both *in vitro* and *in vivo*, prolonged the retention time in the gastrointestinal tract (GIT), and enhanced the permeability across the mucus layer and intestinal epithelial cells to increase oral bioavailability and plaque accumulation of CIN. Validated in an AS mouse model, CIN@DEX_{sk}-BSA/PTM/VB₁₂ achieved prominent therapeutic efficacy combating AS. This study highlights the advantages of DEX_{sk}-BSA/PTM and VB₁₂ in the development of nanoemulsions for CIN and provides a promising oral nanoplatform for the delivery of essential oils.

KEYWORDS: 1,8-cineole, essential oils, protein-polysaccharide, VB₁₂, nanoemulsion, oral delivery, atherosclerosis



Atherosclerosis (AS) is a chronic inflammatory disease caused by lipid deposition in the vascular wall leading to plaque formation, which is the pathological basis of cardiovascular and cerebrovascular diseases, including coronary heart disease, cerebral stroke, and arterial occlusion.^{1–3} The progression of AS is primarily associated with abnormal serum lipid metabolism, oxidative stress, and inflammatory responses that induce endothelial injury and subsequent plaque formation.^{4,5} In previous studies, including ours, an essential oil monomer-1,8-cineole has been verified to have antioxidant and anti-inflammation effects on the alleviation of acute inflammation and hyperglycemia-induced endothelial injury.^{6–9} Given that CIN also affected the regulation of cholesterol metabolism, it was speculated that CIN might be a potential drug for the treatment of AS.¹⁰

Oral administration has considerable advantages in safety, convenience, and patient compliance and is regarded as the foremost administer approach, especially for chronic diseases.¹¹ However, it remains challenging to orally administrate essential oils because of their low hydrophilicity, high volatility, and instability in the harsh gastrointestinal tract (GIT) environment.⁹ A few reports have described the development of an oral formulation of CIN, including liposomes, lipid nanoparticles, and a self-microemulsifying drug delivery

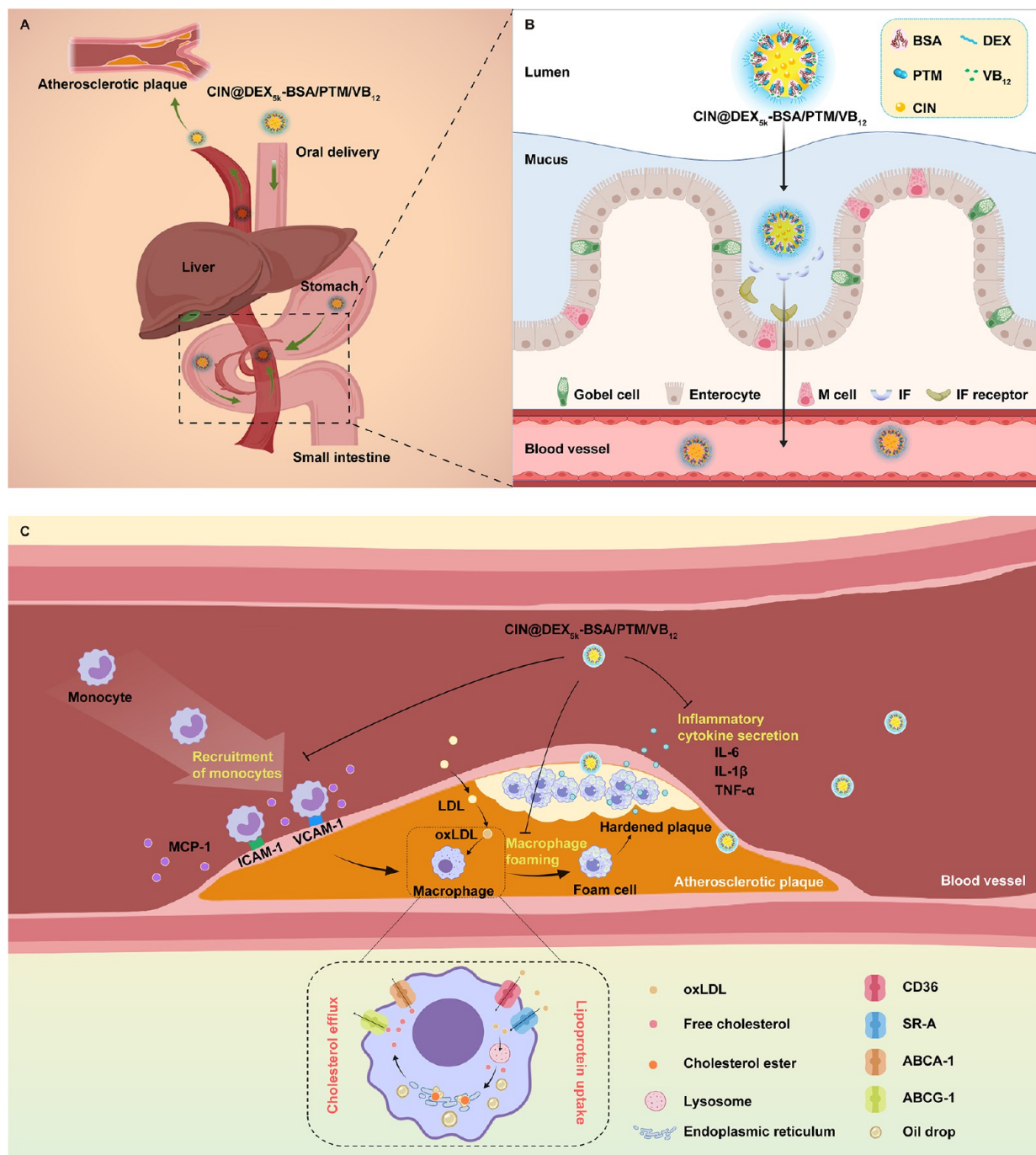
Received: December 8, 2022

Accepted: May 8, 2023

Published: May 12, 2023



Scheme 1. CIN@DEX_{5k}-BSA/PTM/VB₁₂ Is Orally Administrated and Successfully Overcomes GIT Barriers with Targeted Accumulation at Atherosclerotic Plaques⁴⁷



⁴⁷The anti-atherosclerotic effect of CIN@DEX_{5k}-BSA/PTM/VB₁₂ may be attributed to the improved cholesterol efflux and downregulated levels of atherosclerotic mediators and inflammatory cytokines.

system.^{6,9,12} However, understanding of the bioavailability of CIN and the *in vivo* biodistribution of formulations after oral administration remains limited. Therefore, the development of a more effective oral drug delivery system (ODDS) for CIN and further study on the stability, retention time in the GIT, permeability across the small intestine, and pharmacokinetics of CIN are necessary.

Nanoemulsions exhibit considerable potential for the encapsulation of essential oils, thereby improving the hydrophilicity and stability of essential oils.^{13–15} Essential oils are

loaded in the internal oil phase of nanoemulsions, which reduces their volatility and degradation *in vitro* and *in vivo*.^{16–18} The emulsifier is the key factor in the preparation of nanoemulsions. Accumulating evidence proved that bovine serum albumin (BSA) is an important emulsifier for preparing nanoemulsions that possess good biocompatibility and biodegradability.^{19,20} Specifically, BSA can spread on the oil–water interface via reconfiguration. The hydrophobic region of BSA is enriched in the oil phase, while the hydrophilic region is exposed to the water phase, forming a viscoelastic interface.²¹

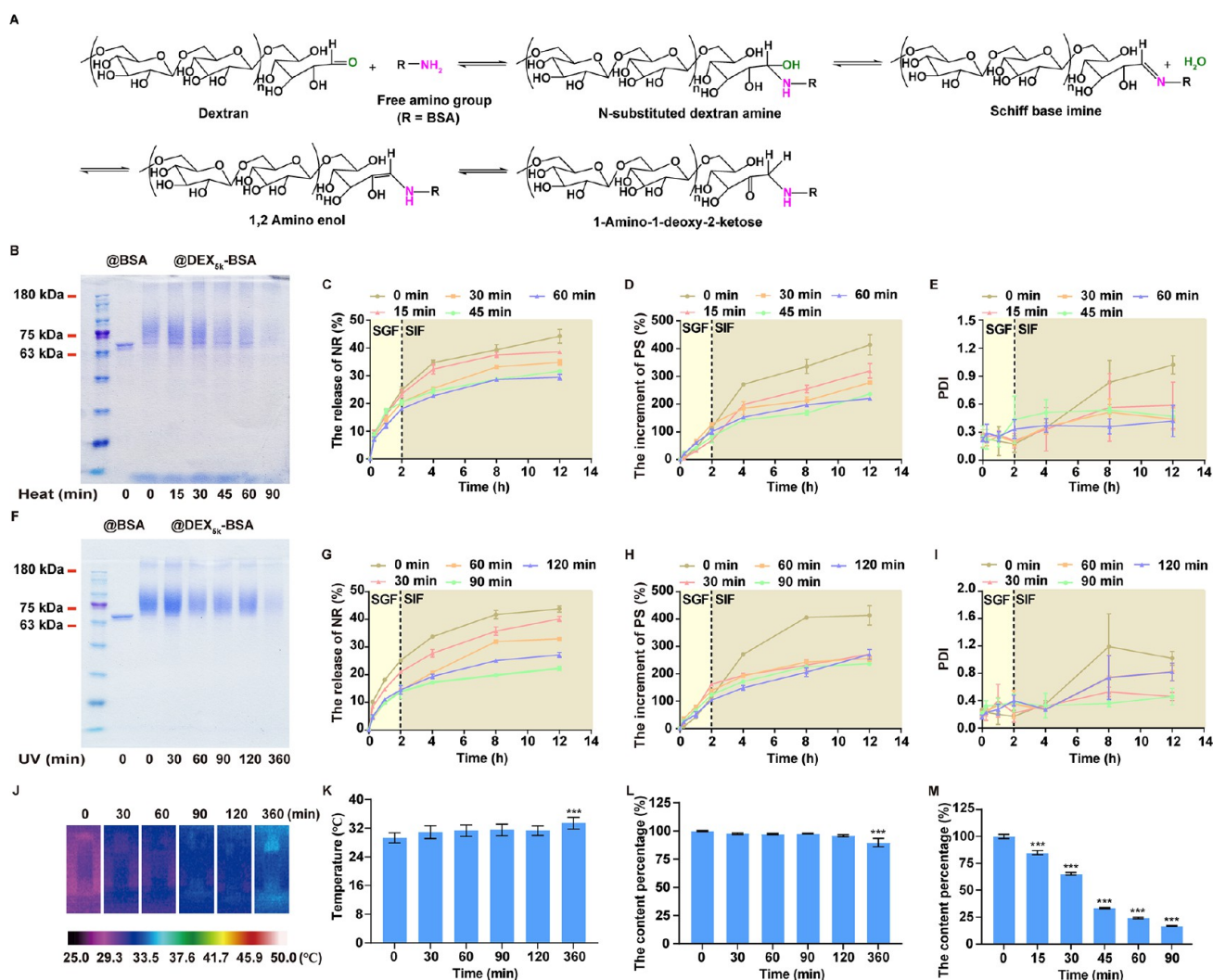


Figure 1. (A) Schematic illustration of DEX-BSAs synthesis through the Maillard reaction. (B) SDS-PAGE patterns of @BSA and @DEX_{sk}-BSA after heat treatment at 90 °C. (C) NR releases, (D) PS, and (E) PDI changes of @DEX_{sk}-BSAs after heat treatment at 90 °C ($n = 3$). (F) SDS-PAGE patterns of @BSA and @DEX_{sk}-BSA after UV irradiation at 36 W. (G) NR releases, (H) PS and (I) PDI changes of @DEX_{sk}-BSAs after UV irradiation at 36 W ($n = 3$). (J) Thermographic maps, (K) temperature, and (L) drug content percentages of CIN@DEX_{sk}-BSAs after UV irradiation at 36 W for different times ($n = 3$). (M) Drug content percentages of CIN@DEX_{sk}-BSAs after heat treatment at 90 °C for different times ($n = 3$). *** $p < 0.001$ compared with 0 min. Each bar represents the mean \pm SD.

However, the interface of a nanoemulsion stabilized by BSA may be considerably affected by environmental factors such as pH, ionic strength, temperature, *etc.*²² The BSA conjugates with a high volume ratio of the hydrophilic unit may exhibit improved stability and emulsifying capacity.^{23,24} Given that polysaccharides are good candidates for hydrophilic units in these BSA conjugates that provide steric hindrance via their hydrophilic chain, polysaccharide-BSA conjugates may be superior emulsifiers than BSA alone in the preparation of nanoemulsion. Dextran (DEX) has been reported to target macrophages in atherosclerotic plaques, and DEX-BSA conjugates may be promising emulsifiers to prepare an oral nanoemulsion for AS treatment.^{25,26} Furthermore, nanoformulations with a neutrally charged surface are preferred for oral delivery.²⁷ Using a positively charged protein to form the DEX-BSA/protein complex could be a good strategy to obtain an electroneutral nanoemulsion. Active Ingredient (PTM) is a positively charged protein that is approved by the Food and Drug Administration (FDA) for clinical use. PTM is usually combined with negative proteins and polysaccharides to

prepare formulations, for instance, neutral PTM Hagedorn Active Ingredient and PTM-neutralized Active Ingredient-like anticoagulant.^{28,29} Therefore, in this study, PTM was used to form a polysaccharide-protein/protein complex with DEX-BSA for the preparation of CIN-loaded oral nanoemulsions.

The bioavailability of a drug is determined by its absorption, which is closely related to its pharmacological effects. It is challenging to transport CIN across the small intestinal epithelium. The physiological barriers in the small intestine include the mucus layer, intestinal epithelial cells (IECs), and submucosal lamina propria, which effectively resist invasion from xenobiotics.³⁰ Nanocarriers have been designed to escape mucus capture and enable transport across IECs and submucosal lamina propria to improve absorption.^{32,33} Although hydrophilicity and electroneutrality endowed the nanocarriers with high permeability across the mucus layer, the hydrophilic surface significantly reduced interactions between the nanocarriers and IECs, resulting in poor epithelial cell transportation.³⁴ Vitamin B12 (VB₁₂) has been shown to bind with intrinsic factor (IF) and enable transport across the

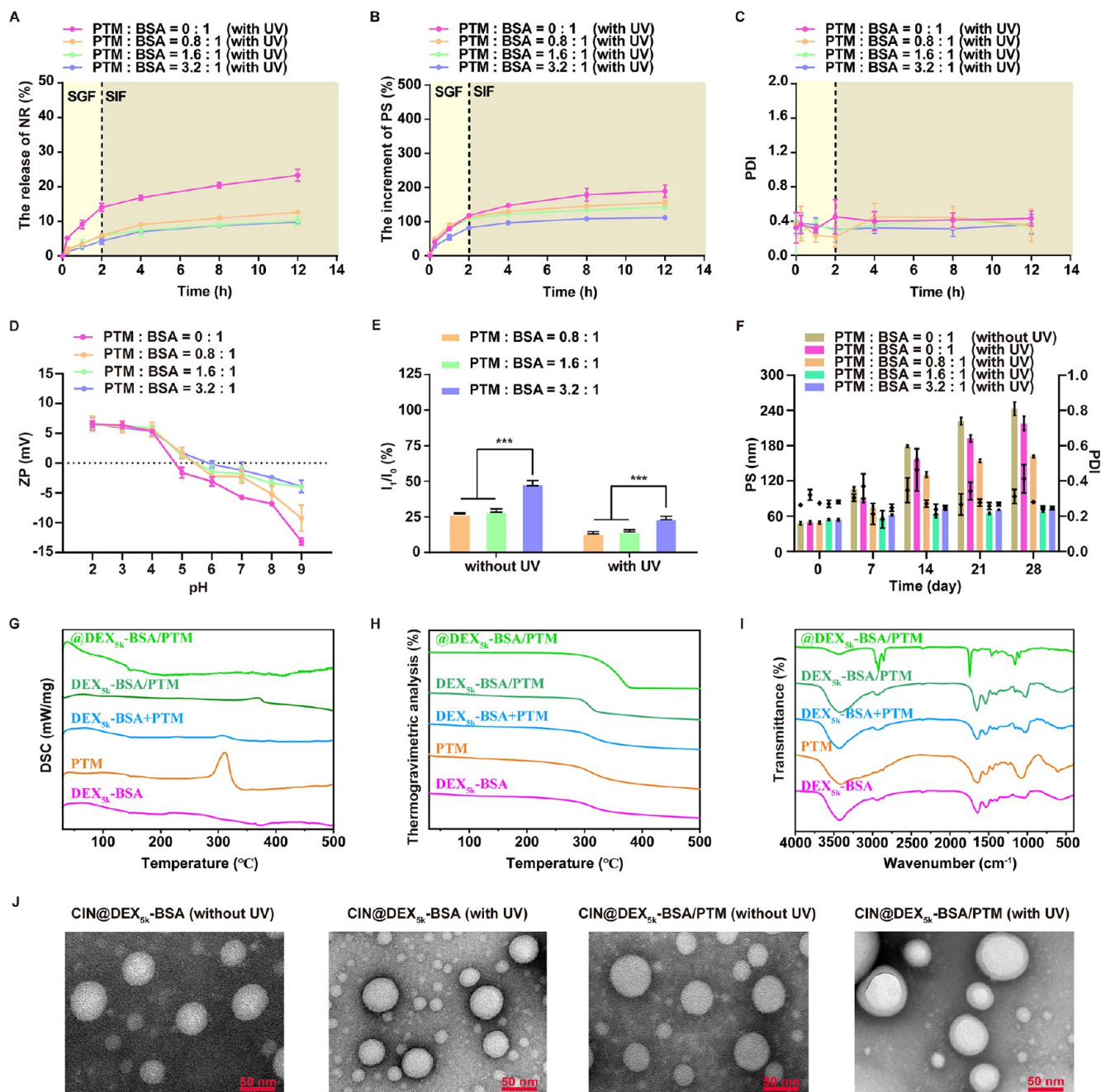


Figure 2. (A) NR releases, (B) PS and (C) PDI changes of @DEX_{5k}-BSA/PTMs with or without UV irradiation ($n = 3$). (D) ZP of @DEX_{5k}-BSA/PTMs prepared at various pH from 2 to 9 ($n = 3$). (E) The unbounded ratio of PTM-FITC in @DEX_{5k}-BSA/PTM-FITC prepared at pH 7 indicated by I_1/I_0 ($n = 3$). *** $p < 0.001$ compared with PTM:BSA = 3.2:1. (F) PS and PDI changes of @DEX_{5k}-BSA/PTMs at 4 °C for 28 days ($n = 3$). Physicochemical properties of @DEX_{5k}-BSA/PTM, DEX_{5k}-BSA/PTM, DEX_{5k}-BSA+PTM, PTM, and DEX_{5k}-BSA were respectively characterized by (G) DSC, (H) thermogravimetric analysis, and (I) FT-IR. (J) TEM images of CIN@DEX_{5k}-BSA and CIN@DEX_{5k}-BSA/PTM with or without UV irradiation (scale bar 50 nm). Each bar represents the mean \pm SD.

intestinal epithelium via IF receptor-mediated cellular uptake at the ileum, suggesting that this could be used as a ligand to improve oral bioavailability.^{35–38} The surface modification of VB₁₂ has been verified to increase the cellular uptake of nanoparticles, liposomes, and polymeric micelles by IECs and thus improve the bioavailability of small molecules and peptides after oral administration.^{39–41} Moreover, the lack of VB₁₂ induces the increment in unmetabolized homocysteine that promotes local inflammation at the endothelial layer, and supplementation of VB₁₂, which is beneficial to the decomposition of homocysteine, prevents the progression of

AS.⁴² Collectively, modification of the surface of nanoemulsion with VB₁₂ may “kill two birds with one stone” to enhance transportation across the epithelial layer and stabilize atherosclerotic plaques.

Herein, we developed a CIN-loaded oral nanoemulsion composed of DEX-BSA conjugate, PTM, and VB₁₂, named CIN@DEX-BSA/PTM/VB₁₂ to combat AS (Scheme 1). A typical microjet method was used to prepare nanoemulsions as this can obtain emulsion droplets of the required small and uniform size with favorable reproducibility. Particularly, the lower temperature favors formulations of CIN and was

controlled throughout the preparation process. The GIT stability, mucus permeability, and retention time of CIN-loaded nanoemulsions were evaluated. Furthermore, the transportation across IECs and atherosclerotic plaque accumulation of nanoemulsion were studied. *In vivo* validation was performed with an AS mouse model, and the therapeutic effect of CIN-loaded oral nanoemulsion was systematically evaluated, and the therapeutic mechanisms of CIN on AS were investigated both *in vivo* and *in vitro*.

RESULTS AND DISCUSSION

Optimization of CIN@DEX_{5k}-BSA. A nanoemulsion composed of DEX-BSA, PTM, VB₁₂, and medium-chain triglyceride (MCT) was developed for the oral delivery of CIN. A series of DEX-BSA conjugates were synthesized by a green and safe Maillard reaction (Figure 1A). DEX-BSAs synthesized at different molecular weights of DEX and under various pH conditions were measured *via* SDS-PAGE (Figure S1). BSA showed a single band around 63 to 75 kDa (Figure S1A). After a 24 h reaction, a smeared band appeared between 75 and 180 kDa, indicating a mixture of DEX-BSAs (Figure S1B). The conjugation degree of DEX-BSAs was quantified and calculated by the *o*-phthalaldehyde (OPA) method (Figure S1C), which showed that as the molecular weight of DEX increased, the conjugation degree steadily decreased. The highest conjugation degree was detected at pH 6 in DEX_{5k}-BSA and reached 30.70%. Nile red (NR)-loaded nanoemulsions were prepared to evaluate the emulsifying capacity of DEX-BSA (Table S1). The leakage rate of the NR@DEX-BSAs emulsion was determined, and the high conjugation degree of DEX contributed to the stability of the nanoemulsion (Figure S1D). The nanoemulsion prepared by DEX_{5k}-BSA exhibited the lowest leakage of NR and was used in the following study.

Protein emulsifiers are known to form a stable interfacial film on the surface of emulsion droplets under heat treatment because of the gel phase transition.^{29,43} This heat-induced gelation comprises two steps. The first step involves heat-induced dissociation and denaturation of the protein, while the second step is the protein–protein interaction phase. Buried sulfhydryl groups can also initiate the disulfide-sulfhydryl exchange reaction to promote cross-linking formation.⁴⁴ This stable interfacial film can prevent proteins adsorbed on the oil–water interface from being replaced by endogenous surface-active molecules and make emulsions more resistant to pH and ionic strength variations.⁴⁵ SDS-PAGE study showed that the band color of the @DEX_{5k}-BSA faded with prolonged heating (Figure 1B). Since protein gelation caused by cross-linking creates an insoluble three-dimensional network, this prevents depolymerization by SDS and β -mercaptoethanol and restricts penetration through the running gel, resulting in lighter bands.^{46,47} Thus, the heat treatment-induced cross-linking between BSA resulted in gelation with time. Correspondingly, the improved stability of @DEX_{5k}-BSA under heat treatment was confirmed by the retarded drug release and reduced variation in particle size (PS) and polydispersity index (PDI) (Figure 1C–E). Although heat treatment could increase the stability of nanoemulsion, it is unsuitable for CIN-loaded emulsions because of the volatility and instability of essential oils at high temperatures. Intriguingly, ultraviolet (UV) irradiation could also denature the proteins to induce cross-linking and could take the place of heat treatment to obtain an interfacial modification of @

DEX_{5k}-BSA. After 60 min of UV irradiation, the BSA gelation was obviously formed in @DEX_{5k}-BSA, as indicated by the SDS-PAGE analysis (Figure 1F). The mechanisms of UV-induced gelation are different from those of heat-induced gelation. The abundance of chromophores endows proteins with photoreactivity, which induces reactions with other excited state species. As a result, side-chain oxidation, backbone fragmentation, cross-linking, and protein aggregates formation lead to an insoluble three-dimensional network.⁴⁸ Similar to the results of heat treatments, the stability of @DEX_{5k}-BSA increased over time because of prolonged UV irradiation exposure, as indicated by the retarded drug release and reduced increment on PS and PDI (Figure 1G–I). Given that the temperature of emulsions undergoes minimal change within 120 min under UV irradiation, this might not affect the stability of CIN in the emulsion (Figure 1J,K). Compared with the heat treatment, UV irradiation did not affect the content of CIN in the emulsion (Figure 1L,M). Therefore, UV irradiation for 90 min was used to increase the stability of CIN@DEX_{5k}-BSA.

Optimization of CIN@DEX_{5k}-BSA/PTM. To produce an electroneutral nanoemulsion, PTM was involved in the formation of an emulsifier. The strong electrostatic interactions between BSA and PTM produced a DEX_{5k}-BSA/PTM emulsifier. NR@DEX_{5k}-BSA/PTM prepared with various molar ratios of PTM/BSA was evaluated (Figure 2A–C). The addition of PTM retarded the release of NR and reduced the variety of emulsions in the simulated GIT medium for PS and PDI. The increased stability of the emulsion may be attributed to its resilience against pH variation because of the relatively large pH difference between simulated gastric fluid (SGF) and simulated intestinal fluid (SGF). The zeta potential (ZP) of @DEX_{5k}-BSA/PTMs was measured in media at various pH values (Figure 2D). The variation of ZP remained narrow as the molar ratio of PTM/BSA increased, which demonstrated that PTM endowed the emulsion with pH buffer capability. To optimize the molar ratio of PTM/BSA, a FITC-labeled PTM (PTM-FITC) was synthesized to quantify the amount of uncombined PTM. For free PTM-FITC, the fluorescence intensity (FL) ratio after and before ultrafiltration (I_1/I_0) was $95.17 \pm 1.25\%$, indicating the complete separation of free PTM-FITC. The I_1/I_0 ratio of @DEX_{5k}-BSA/PTM-FITC was evaluated at different molar ratios of PTM/BSA (Figure 2E). A sharp increase in I_1/I_0 at the PTM/BSA molar ratio of 3.2:1, suggested that the binding between PTM and BSA was saturated at the ratio of 1.6:1. Intriguingly, UV irradiation further improved the binding capacity, as indicated by the reduced I_1/I_0 ratio, which may be attributed to the gel formation between BSA and PTM. The long-term stability of @DEX_{5k}-BSA/PTM was studied for PS (Figure 2F). With UV irradiation, a size increment from 49.06 to 217.96 nm for 28 days at 4 °C was observed in @DEX_{5k}-BSA, whereas PTM involvement reduced the size variation, especially at the PTM/BSA molar ratios of 1.6:1 and 3.2:1. Hence, the PTM/BSA molar ratio of 1.6:1 was used in subsequent experiments.

More detailed properties of @DEX_{5k}-BSA/PTM were provided by differential scanning calorimetry (DSC), thermogravimetric analysis, and Fourier transform infrared spectroscopy (FT-IR) (Figure 2G–I). DEX_{5k}-BSA and PTM exhibited characteristic endothermic peaks at 65 and 311 °C, respectively. The physical mixture of DEX_{5k}-BSA and PTM exhibited characteristic peaks of DEX_{5k}-BSA and PTM at 67 and 307 °C simultaneously, whereas the freeze-dried sample of

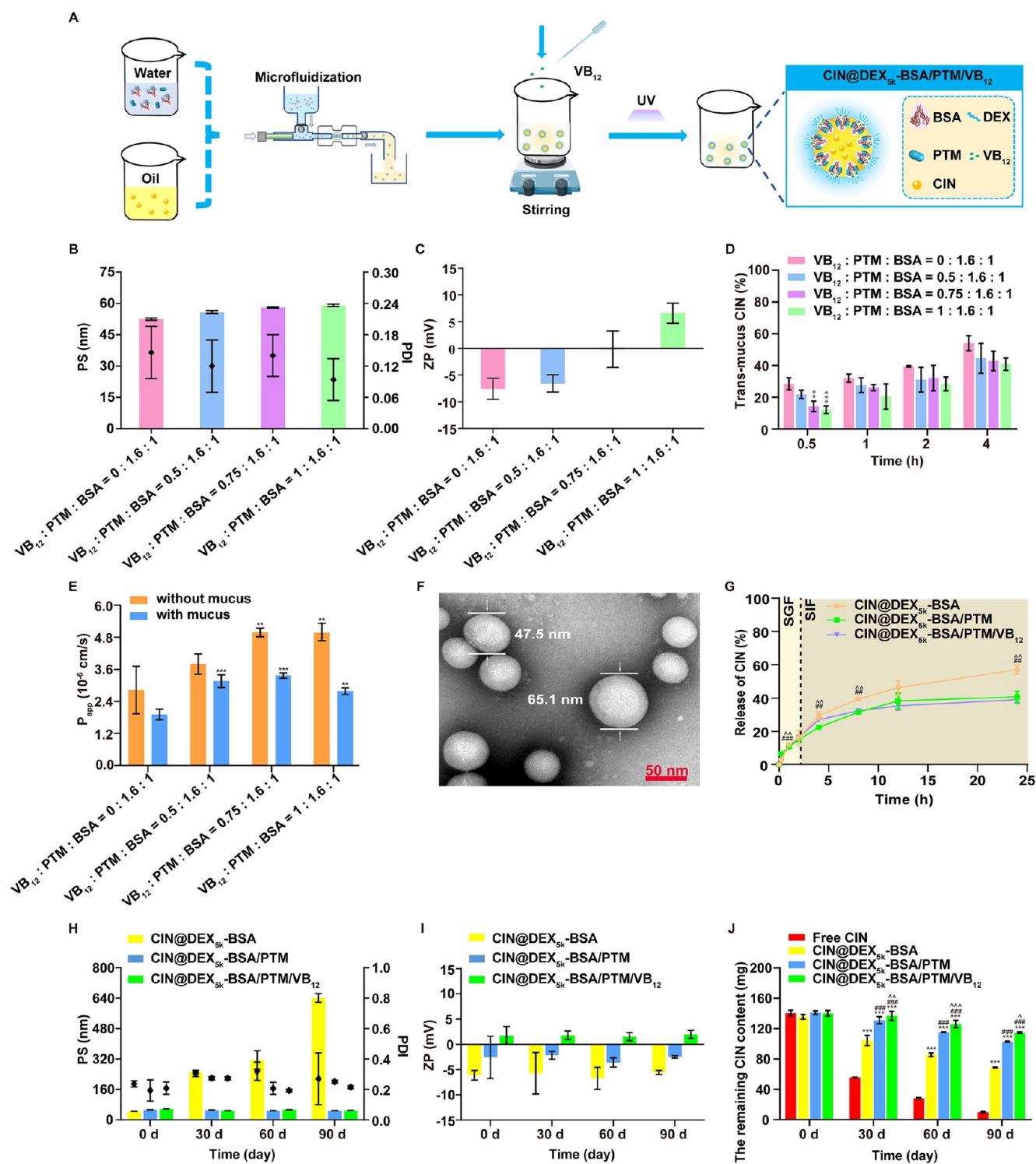


Figure 3. (A) Schematic illustration of the preparation process of CIN@DEX_{sk}-BSA/PTM/VB₁₂. Optimization of VB₁₂ inserted contents for (B) PS and PDI, (C) ZP, (D) mucus permeability, and (E) P_{app} values of Caco-2 cell monolayer ($n = 3$). $**p < 0.01$, $***p < 0.001$ compared with VB₁₂:PTM:BSA = 0:1.6:1. (F) TEM image of CIN@DEX_{sk}-BSA/PTM/VB₁₂ (scale bar 50 nm). (G) *In vitro* drug release profile of CIN from CIN@DEX_{sk}-BSA, CIN@DEX_{sk}-BSA/PTM, and CIN@DEX_{sk}-BSA/PTM/VB₁₂ in SGF and SIF ($n = 3$). (H) PS and PDI, (I) ZP changes of CIN@DEX_{sk}-BSA, CIN@DEX_{sk}-BSA/PTM, and CIN@DEX_{sk}-BSA/PTM/VB₁₂ storage at 4 °C for 90 days. (J) The remaining CIN content in free CIN, CIN@DEX_{sk}-BSA, CIN@DEX_{sk}-BSA/PTM, and CIN@DEX_{sk}-BSA/PTM/VB₁₂ within 90 days ($n = 3$). $**p < 0.001$ compared with free CIN group; $###p < 0.001$ compared with CIN@DEX_{sk}-BSA; $^{\wedge}p < 0.05$, $^{\wedge\wedge}p < 0.01$, $^{\wedge\wedge\wedge}p < 0.001$ compared with CIN@DEX_{sk}-BSA/PTM. Each bar represents the mean \pm SD.

DEX_{sk}-BSA/PTM possessed a shift of the characteristic peak of PTM to 370 °C, indicating the strong combination between DEX_{sk}-BSA and PTM. After UV irradiation on DEX_{sk}-BSA/

PTM, the characteristic peak of PTM was covered, which may be caused by the cross-linking between DEX_{sk}-BSA/PTM. Thermogravimetric curves illustrated the mass change of

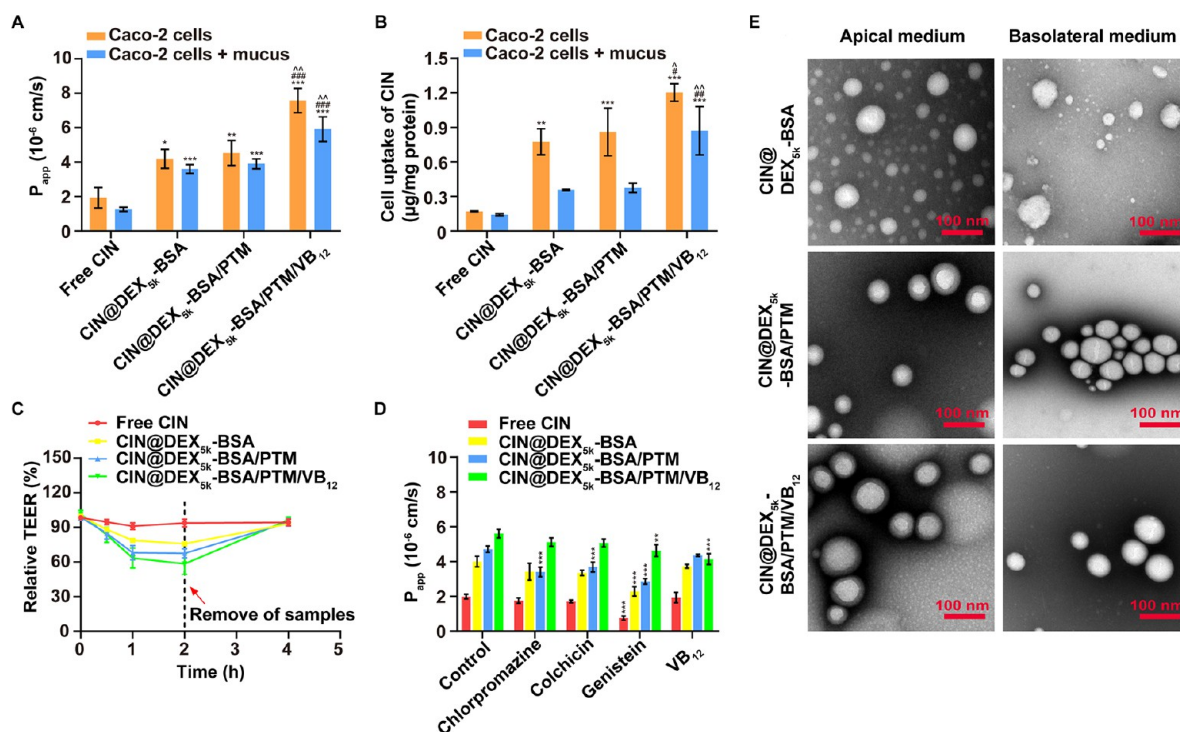


Figure 4. (A) P_{app} values of CIN preparations in Caco-2 cell monolayer with or without mucus at 2 h ($n = 3$). (B) Cellular uptake of CIN preparations in Caco-2 cell monolayer with or without mucus at 1 h ($n = 3$). $*p < 0.05$, $**p < 0.01$, $***p < 0.001$ compared with free CIN group; $\#p < 0.05$, $\#\#p < 0.01$, $\#\#\#p < 0.001$ compared with CIN@DEX_{5k}-BSA; $\wedge p < 0.05$, $\wedge\wedge p < 0.01$ compared with CIN@DEX_{5k}-BSA/PTM. (C) Relative TEER changes of the Caco-2 cell monolayer after treatment by CIN preparations ($n = 3$). (D) P_{app} values of CIN preparations in Caco-2 cell monolayer under different inhibitory conditions ($n = 3$). $**p < 0.01$, $***p < 0.001$ compared with control group. (E) TEM images for CIN@DEX_{5k}-BSA, CIN@DEX_{5k}-BSA/PTM, and CIN@DEX_{5k}-BSA/PTM/VB₁₂ at both the apical side and basolateral side of Caco-2 cell monolayer (with mucus) after incubating in MEM at 37 °C for 2 h. Each bar represents the mean \pm SD.

components during the heating process. A mass change at 310 °C was detected in all the groups, caused by protein degradation. The temperature range is prolonged in @DEX_{5k}-BSA/PTM, which is closely related to the gel phase of proteins. For FT-IR spectra, only @DEX_{5k}-BSA/PTM after UV irradiation exhibited different absorption bands at 2930.71, 1654.4, and 1020.11 cm^{-1} , which were caused by the stretching vibration of C–H bonds from saturated methyl and methylene groups, vibronic couplings between N–H bending and C–N stretching of amide groups, and the stretching vibration of the glycosidic bond, respectively. Collectively, DEX_{5k}-BSA and PTM may form a stable combination that was further enhanced by the UV irradiation.

The morphology of CIN-loaded emulsions with and without UV irradiation was observed using transmission electron microscopy (TEM) (Figure 2J). In CIN@DEX_{5k}-BSA, spherical particles of approximately 50 nm in size were observed regardless of the UV irradiation. However, a hydration layer was clearly observed on the surface of CIN@DEX_{5k}-BSA/PTM after UV irradiation. It is supposed that the combination of BSA and PTM favors cross-linking under UV irradiation, facilitating the stretching of DEX on the oil–water interface, which might be the reason for the enhanced stability.

Preparation and Characterization of CIN@DEX_{5k}-BSA/PTM/VB₁₂. The preparation process of CIN@DEX_{5k}-BSA/PTM/VB₁₂ emulsion is illustrated in Figure 3A. As VB₁₂ can facilitate transepithelial absorption and accumulation at atherosclerotic plaques, it was absorbed on the surface of the nanoemulsion before UV irradiation. With the increasing molar ratio of VB₁₂, the binding efficiency of VB₁₂ in the

nanoemulsions improved (Table S2). The addition of VB₁₂ slightly increased the PS of CIN@DEX_{5k}-BSA/PTM/VB₁₂, while this induced a charge reversal at the VB₁₂/PTM/BSA molar ratio of 1:1.6:1 (Figure 3B,C). To evaluate the permeability of the nanoemulsions across small epithelial cells *in vitro*, a transwell system was used with mucus or a Caco-2 cell monolayer in the upper chamber. VB₁₂ slightly reduced the penetration of CIN across the mucus (Figure 3D), which may be closely related to the interactions between nanoemulsions with positive potential and mucus. However, VB₁₂ enhanced the permeation of CIN through the Caco-2 cell monolayer, as indicated by an increased apparent permeability (P_{app}) value (Figure 3E), which was attributed to VB₁₂–IF complex mediated cellular uptake. Although a reduced P_{app} value was measured in a mucus/Caco-2 cell multilayer model, CIN@DEX_{5k}-BSA/PTM/VB₁₂ notably possessed a higher P_{app} value than that of CIN@DEX_{5k}-BSA/PTM. The emulsion prepared at a VB₁₂/PTM/BSA molar ratio of 0.75:1.6:1 exhibited a 1.45-fold higher P_{app} value than that of the CIN@DEX_{5k}-BSA/PTM group and was subsequently used in the following experiments.

The morphology of CIN@DEX_{5k}-BSA/PTM/VB₁₂ was observed (Figure 3F) and was similar to that of CIN@DEX_{5k}-BSA/PTM. However, the chemical elements at a depth of 1–10 nm below the surface of nanoemulsion droplets analyzed by an X-ray photoelectron spectrometer (XPS) indicated the presence of VB₁₂ by the enhanced mass concentration of Co (Table S3). The PS, PDI, ZP, loading efficiency (LE), and loading capability (LC) of CIN@DEX_{5k}-BSA, CIN@DEX_{5k}-BSA/PTM, and CIN@DEX_{5k}-BSA/PTM/

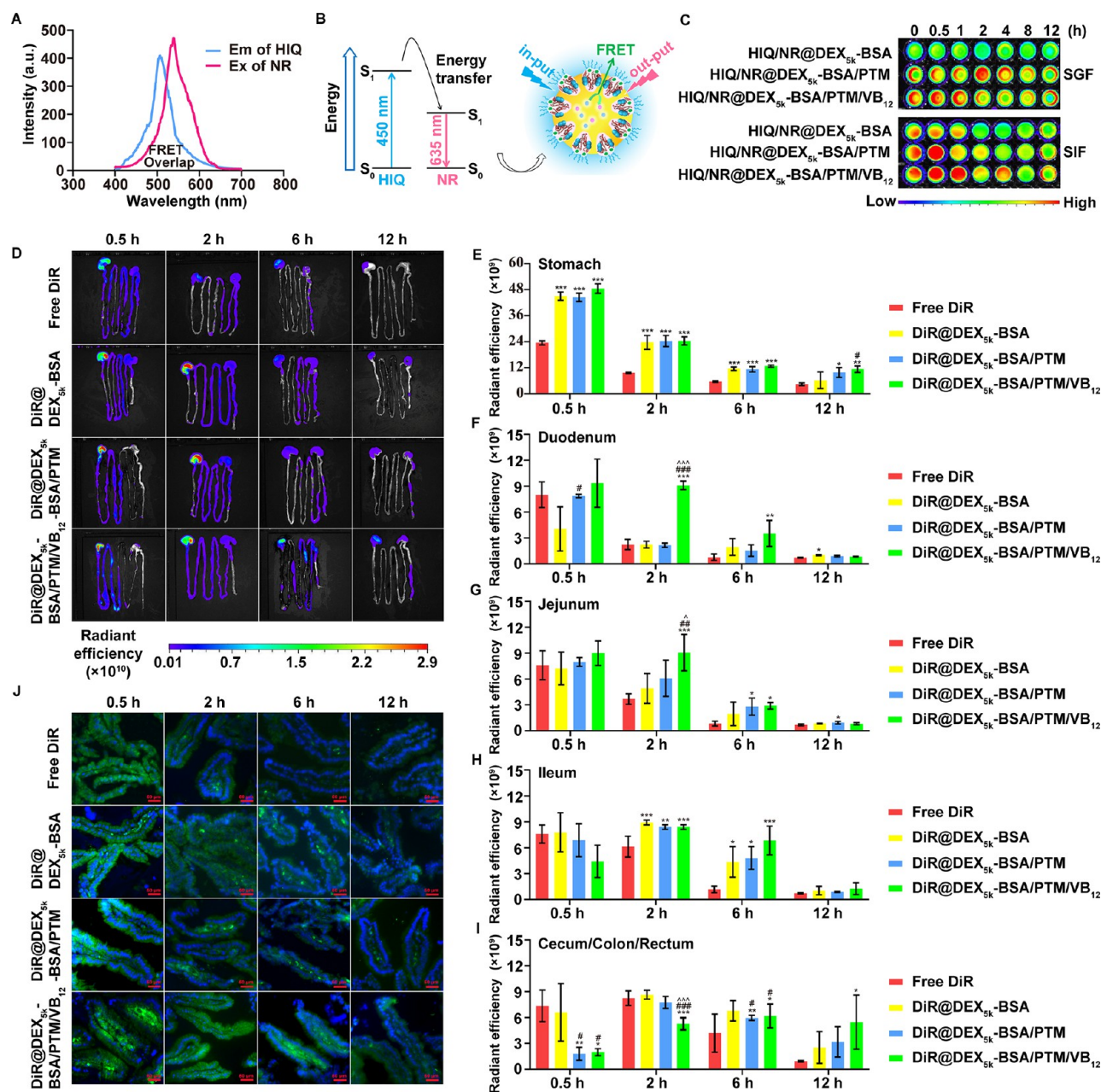


Figure 5. (A) Emission spectrum of HIQ and excitation spectrum of the NR receptor. (B) Illustration of FRET effect between HIQ and NR. (C) FRET technology for studying the stability of HIQ/NR@DEX_{5k}-BSA, HIQ/NR@DEX_{5k}-BSA/PTM, and HIQ/NR@DEX_{5k}-BSA/PTM/VB₁₂ in the SGF and SIF within 12 h. (D–I) Fluorescent signals of free DiR, DiR@DEX_{5k}-BSA, DiR@DEX_{5k}-BSA/PTM, and DiR@DEX_{5k}-BSA/PTM/VB₁₂ in the GIT at various time points after oral administration ($n = 4$). * $p < 0.05$, ** $p < 0.01$, *** $p < 0.001$ compared with free DiR group; # $p < 0.05$, ## $p < 0.01$, ### $p < 0.001$ compared with DiR@DEX_{5k}-BSA; ^ $p < 0.05$, ^^ $p < 0.001$ compared with DiR@DEX_{5k}-BSA/PTM. (J) Representative fluorescence images of mice ileal segments after oral administration of DiR preparations. DiR is shown in green, and nuclei of cells are shown by the blue color (DAPI stained). Scale bar 50 μm . Each bar represents the mean \pm SD.

VB₁₂ were measured (Table S4). Both CIN@DEX_{5k}-BSA/PTM and CIN@DEX_{5k}-BSA/PTM/VB₁₂ showed a considerably retarded release and reduced cumulative release of CIN at 24 h (reduced by 16.45% and 18.73%) compared with that of CIN@DEX_{5k}-BSA (Figure 3G), indicating the improved stability of the emulsion in SGF and SIF. Furthermore, the stability of emulsions was studied for 90 days at 4 °C (Figure 3H–J). CIN@DEX_{5k}-BSA/PTM and CIN@DEX_{5k}-BSA/PTM/VB₁₂ exhibited no discernible change in appearance, whereas CIN@DEX_{5k}-BSA underwent delamination at 90 days (Figure S3). Correspondingly, a continuously growing PS of

CIN@DEX_{5k}-BSA was detected within 90 days, whereas no variation in the PS was observed in CIN@DEX_{5k}-BSA/PTM or CIN@DEX_{5k}-BSA/PTM/VB₁₂. Furthermore, no apparent change was observed in the ZP of all emulsions. As an essential oil monomer, the content loss of CIN due to volatilization and degradation is a crucial problem. The content of free CIN showed more than 92% loss after 90 days of storage. CIN@DEX_{5k}-BSA prevented the loss of CIN to some extent and preserved 50% of the total drug content. CIN@DEX_{5k}-BSA/PTM and CIN@DEX_{5k}-BSA/PTM/VB₁₂ remained more than 70% and 80% of the total drug, respectively, which was

significantly higher than the amount of free CIN retained (7.12% remaining). DEX_{5k}-BSA could not stabilize the oil–water interface of droplets in the nanoemulsion, and these were inclined to merge and aggregate. The strong combination between PTM and BSA that was further strengthened by UV irradiation contributed to the superior stability of CIN@DEX_{5k}-BSA/PTM and CIN@DEX_{5k}-BSA/PTM/VB₁₂. Collectively, @DEX_{5k}-BSA/PTM/VB₁₂ holds considerable promise in achieving efficient oral delivery of CIN.

Permeation Across the Mucus Layer and Caco-2 Cell Monolayer. To evaluate the transportation of CIN across IECs, the P_{app} value of CIN through the Caco-2 cell monolayer was evaluated (Figure 4A). Nanoemulsions improved the permeation of CIN by 2–3 folds compared with that of free CIN, especially for CIN@DEX_{5k}-BSA/PTM/VB₁₂. Consistent with the trans-mucus permeability results (Figure 3D), the mucus/Caco-2 cell multilayer reduced the permeation of CIN and its nanoemulsions. Both transepithelial transcytosis and paracellular transportation may contribute to the permeation of CIN. The transcellular pathway includes endocytosis and basement membrane release in sequence. To discover the role of the transcellular pathway in the permeation of CIN, Caco-2 cellular uptake was measured (Figure 4B). All nanoemulsions significantly improved the cellular uptake of CIN in comparison with that of free CIN. Although the mucus layer reduced the cellular uptake of CIN regardless of the nanoemulsions, CIN@DEX_{5k}-BSA/PTM/VB₁₂ exhibited the highest cellular uptake among all the groups. It was supposed that VB₁₂-IF mediated cellular uptake facilitated CIN penetration *via* a transcellular pathway. In addition, paracellular transportation was evaluated using transepithelial electrical resistance (TEER) detection (Figure 4C). All CIN nanoemulsions at the apical side of cell monolayers immediately reduced TEER and gradually restored this after the removal of the preparations, in contrast with free CIN that maintained a constant TEER value, indicating the instant and reversible opening of the tight junctions. Hence, paracellular transportation also contributed to the penetration of CIN nanoemulsions. Moreover, the penetration mechanisms of CIN nanoemulsions across the Caco-2 cell monolayer were investigated (Figure 4D). P_{app} values of CIN@DEX_{5k}-BSA and CIN@DEX_{5k}-BSA/PTM were reduced following treatment with Active Ingredient, Active Ingredient, and genistein, indicating that clathrin-mediated endocytosis, caveolin-mediated endocytosis, and micropinocytosis contributed to the penetration of nanoemulsions. Although the P_{app} value of CIN@DEX_{5k}-BSA/PTM/VB₁₂ varied slightly, which may be caused by the offset of VB₁₂-IF mediated cellular uptake. The addition of VB₁₂ significantly decreased the P_{app} value of CIN@DEX_{5k}-BSA/PTM/VB₁₂ but did not affect those of CIN@DEX_{5k}-BSA and CIN@DEX_{5k}-BSA/PTM. The competitive inhibitory effect of free VB₁₂ impeded the cellular uptake of CIN@DEX_{5k}-BSA/PTM/VB₁₂ in the presence of IF, suggesting that the transcytosis of CIN@DEX_{5k}-BSA/PTM/VB₁₂ was mediated by IF receptors on the surface of Caco-2 cells. To investigate the integrity of nanoemulsions after penetration, TEM images were captured for CIN@DEX_{5k}-BSA, CIN@DEX_{5k}-BSA/PTM, and CIN@DEX_{5k}-BSA/PTM/VB₁₂ at both the apical and basolateral sides of the Caco-2 cell monolayer after 2 h of incubation (Figure 4E). After passing through the Caco-2 cell monolayer (with mucus), CIN@DEX_{5k}-BSA showed increased PS and PDI (Figure S4). Meanwhile, TEM images of CIN@DEX_{5k}-BSA on the basolateral side showed some unrounded

emulsion droplets, indicating destabilization of the nanoemulsion. Since mucins,⁴⁹ enzymes⁵⁰ and endogenous phospholipids⁵¹ may interfere with the stability of emulsion droplets *via* insertion into the water–oil interface during absorption, the insertion of mucin and lipids into the surface of emulsion droplets could contribute to the morphology transformation of CIN@DEX_{5k}-BSA. The maintained emulsion droplet integrity of CIN@DEX_{5k}-BSA/PTM and CIN@DEX_{5k}-BSA/PTM/VB₁₂ may be closely related to the insertion of PTM, which partly prevents the insertion of endogenous materials, thereby improving stability during transportation.

Retention of @DEX_{5k}-BSA/PTM/VB₁₂ in the GIT. Before the evaluation of the residence time of nanoemulsions in GIT, the stability of nanoemulsions in various simulated media was studied *via* Förster resonance energy transfer (FRET) reagent pairs. 3-hydroxyisoquinoline (HIQ) and NR can be used as the FRET reagent pair as the emission spectrum of HIQ overlaps with the excitation spectrum of NR (Figure 5A). Within the Förster distance, the fluorescence energy can be transferred from the donor-HIQ to the receptor-NR, resulting in emission from NR and weakened emission from HIQ (Figure 5B). HIQ and NR were encapsulated in the oil phase of nanoemulsions and characterized (Table S5). During 12 h of incubation in the SGF and SIF media, the FL of HIQ and NR were captured (Figure 5C), and the FRET ratio was detected (Figure 5S). HIQ/NR@DEX_{5k}-BSA/PTM and HIQ/NR@DEX_{5k}-BSA/PTM/VB₁₂ exhibited greater stability than that of HIQ/NR@DEX_{5k}-BSA in both SGF and SIF, as indicated by the NR fluorescence and FRET ratio.

The retention of 1,1'-diiodo-3,3',3'-tetramethylindocarbocyanine (DiR)-loaded nanoemulsions in the GIT was observed using a small animal *in vivo* optical imaging system (IVIS). After oral administration, the near-infrared light of DiR was captured at predetermined time points (Figure 5D) and the radiant efficiencies at the stomach, duodenum, jejunum, ileum, and cecum/colon/rectum were quantified (Figure 5E–I). Free DiR exhibited fast fecal elimination from the GIT in all groups. DiR@DEX_{5k}-BSA/PTM/VB₁₂ had a longer residence time in the duodenum and jejunum than that of DiR@DEX_{5k}-BSA and DiR@DEX_{5k}-BSA/PTM within 2 h. Although @DEX_{5k}-BSA/PTM possessed favorable stability *in vitro*, a clear difference with @DEX_{5k}-BSA was lacking. Given that @DEX_{5k}-BSA/PTM/VB₁₂ showed a prolonged residence time in the small intestine, especially in the duodenum and jejunum, VB₁₂-IF mediated cellular uptake by epithelial cells could play a decisive role in preventing transit through the GIT. Furthermore, the small intestines were dissected at each time point, and the ileal segments were sliced and observed using a laser confocal microscope (Figure 5J). Free DiR exhibited the highest fluorescence in the ileum microvilli and epithelial cells at 0.5 h, and a weak fluorescence signal was observed at the basolateral side at 2 h. All nanoemulsions exhibited improved cellular uptake and high fluorescence signals at the basolateral side. The fluorescence signal in DiR@DEX_{5k}-BSA/PTM/VB₁₂ was the highest at 6 h and was even detectable at 12 h. This result demonstrated that DiR@DEX_{5k}-BSA/PTM/VB₁₂ effectively promoted the transcytosis of DiR through epithelial cells, which was the prerequisite for high bioavailability.

Pharmacokinetics of CIN and Biodistribution of Nanoemulsions. The bioavailability of CIN after oral administration is the most important assessment criterion for nanoemulsions. Plasma drug concentration–time curves of free CIN and CIN nanoemulsions after oral administration were

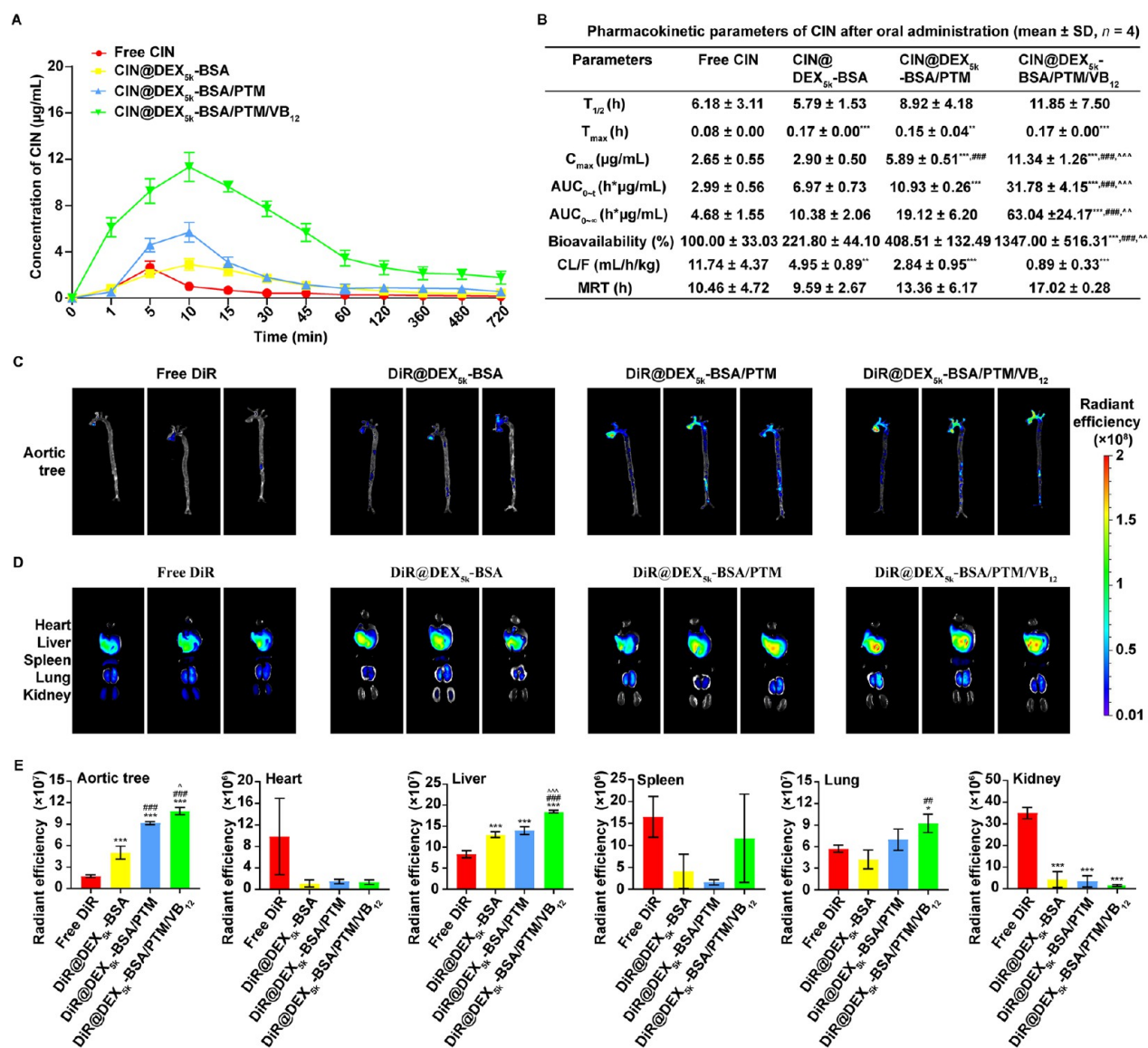


Figure 6. (A) Plasma drug concentration–time curves and (B) major pharmacokinetic parameters of CIN following oral administration of various CIN preparations at a dose of 50 mg/kg in C57BL/6J mice ($n = 4$). ^{**} $p < 0.01$, ^{***} $p < 0.001$ compared with free CIN group; ^{###} $p < 0.001$ compared with CIN@DEX_{5k}-BSA; ^{^^^} $p < 0.01$, ^{^^^} $p < 0.001$ compared with CIN@DEX_{5k}-BSA/PTM. At 12 h after gavage of DiR preparations (2 mg/kg), atherosclerotic mice were euthanized, and (C) aortic trees from every animal were dissected and observed via IVIS. (D) Tissues from every animal were dissected and observed via IVIS. (E) Quantitation of radiant efficiency for aortic trees and tissues ($n = 3$). ^{*} $p < 0.05$, ^{***} $p < 0.001$ compared with free DiR group; ^{##} $p < 0.01$, ^{###} $p < 0.001$ compared with DiR@DEX_{5k}-BSA; [^] $p < 0.05$, ^{^^} $p < 0.001$ compared with DiR@DEX_{5k}-BSA/PTM. Each bar represents the mean \pm SD.

assessed (Figure 6A) and the major pharmacokinetic parameters of CIN were calculated under the noncompartmental model fitting (Figure 6B). In the free CIN group, a maximum plasma concentration (C_{max}) of about 2.65 $\mu\text{g/mL}$ with rapid elimination was observed. CIN@DEX_{5k}-BSA, CIN@DEX_{5k}-BSA/PTM and CIN@DEX_{5k}-BSA/PTM/VB₁₂ improved the area under the concentration–time curve (AUC_{0-∞}) of CIN by 2.22, 4.09, and 13.47 folds, respectively, compared to free CIN. However, CIN@DEX_{5k}-BSA failed to increase the C_{max} of CIN. CIN@DEX_{5k}-BSA/PTM/VB₁₂ exhibited the highest C_{max} and longest half-life ($T_{1/2}$) of CIN among all groups. Thereby, the bioavailability of CIN in CIN@DEX_{5k}-BSA/PTM/VB₁₂ was more than 10 times that of the free CIN group. The superior stability and longer retention in the GIT of @DEX_{5k}-BSA/PTM/VB₁₂ could facilitate the transepithelial transportation of CIN. Furthermore, the

hydrophilic and electroneutral surface of CIN@DEX_{5k}-BSA/PTM/VB₁₂ was not conducive to opsonin absorption and prolonged the circulation time, which is fundamental for accumulation at plaques.

The biodistribution of DiR-loaded nanoemulsions was implemented to assess the plaque targeting capability. After oral administration of free DiR, DiR@DEX_{5k}-BSA, DiR@DEX_{5k}-BSA/PTM, and DiR@DEX_{5k}-BSA/PTM/VB₁₂, mice were euthanized at 12 h. The aortic tree and tissues were imaged (Figure 6C,D) and analyzed (Figure 6E) using IVIS. The fluorescence signals in the free DiR mainly accumulated in the heart, spleen and kidney, indicating the rapid metabolism in the liver and excretion from the kidney at 12 h. Nanoemulsions increased the plaque accumulation of DiR which was closely related to the surface modification. DEX and their derivatives (carboxyl DEX, sulfated DEX, and thiol-DEX)

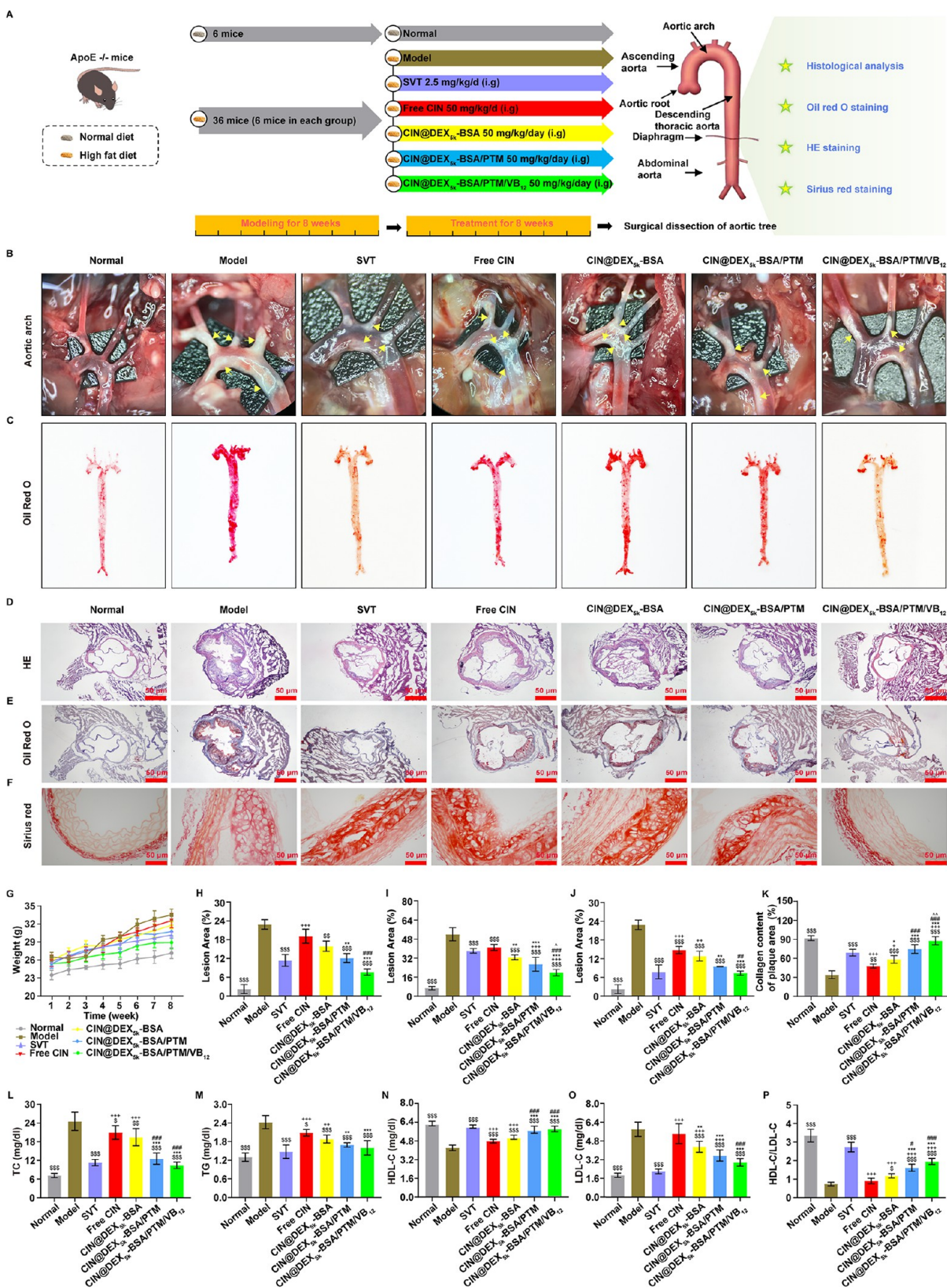


Figure 7. (A) Illustration of ApoE^{-/-} mice grouping and treatment. (B) Plaques (yellow arrows) in the aortic arch of ApoE^{-/-} mice ($n = 6$). (C,H) Atherosclerotic lesion area of the whole aortic tree was analyzed using Oil Red O staining ($n = 3$). Sections of the aortic root were stained with (D,I) HE ($n = 6$), (E,J) Oil Red O ($n = 3$), or (F,K) Sirius red ($n = 6$). Scale bar 50 μm . (G) Comparison of mice body weight ($n = 6$). The serum lipid indicators including (L) TC, (M) TG, (N) HDL-C, (O) LDL-C, and (P) HDL-C/LDL-C at different groups after treatments ($n = 6$). $^*p < 0.05$, $^{**}p < 0.01$, $^{***}p < 0.001$ compared with model group; $^{\#}p < 0.05$, $^{\#\#}p < 0.01$, $^{\#\#\#}p < 0.001$ compared with free CIN group; $^{\wedge}p < 0.05$, $^{\wedge\wedge}p < 0.01$ compared with CIN@DEX_{sk}-BSA/PTM. Each bar represents the mean \pm SD.

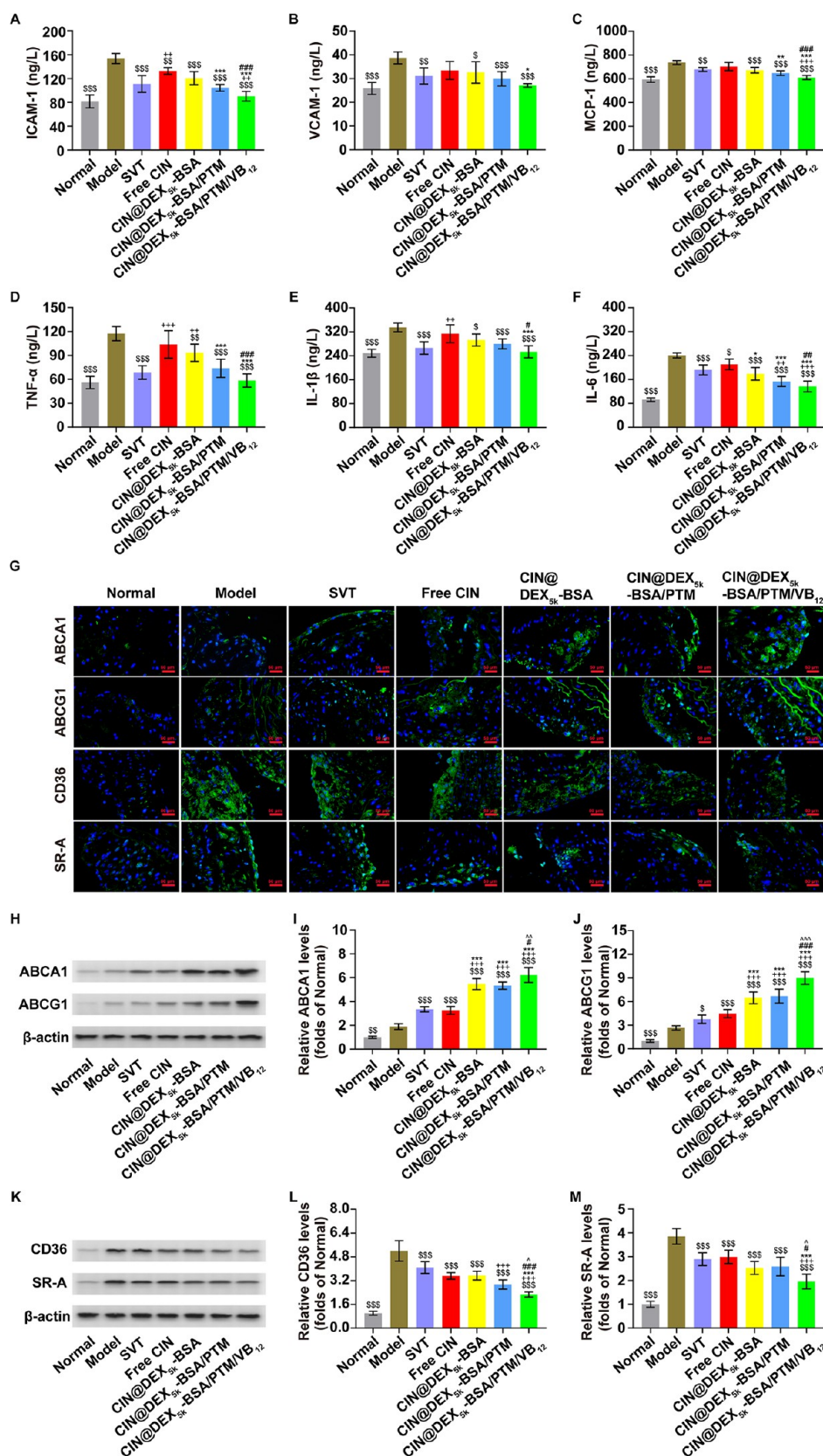


Figure 8. Serum atherosclerotic mediators including (A) ICAM-1, (B) VCAM-1, and (C) MCP-1 and the serum inflammatory cytokines (D) TNF- α , (E) IL-1 β , and (F) IL-6. (G) Immunofluorescence staining (green) of ABCA1, ABCG1, CD36, and SR-A in the aortic root with DAPI counterstaining (blue), scale bar 50 μ m. Western blot analysis of (H–J) ABCA1 and ABCG1 and (K–M) CD36 and SR-A expression in the aorta of ApoE^{-/-} mice. $^{\$}p < 0.05$, $^{\$\$}p < 0.01$, $^{\$ \$ \$}p < 0.001$ compared with model group; $^{++}p < 0.01$, $^{+++}p < 0.001$ compared with SVT group; $^{*}p < 0.05$, $^{**}p < 0.01$, $^{***}p < 0.001$ compared with free CIN group; $^{\#}p < 0.05$, $^{\#\#}p < 0.01$, $^{\#\#\#}p < 0.001$ compared with CIN@DEX_{5k}-BSA; $^{\wedge}p < 0.05$, $^{\wedge\wedge}p < 0.01$, $^{\wedge\wedge\wedge}p < 0.001$ compared with CIN@DEX_{5k}-BSA/PTM. Each bar represents the mean \pm SD ($n = 6$).

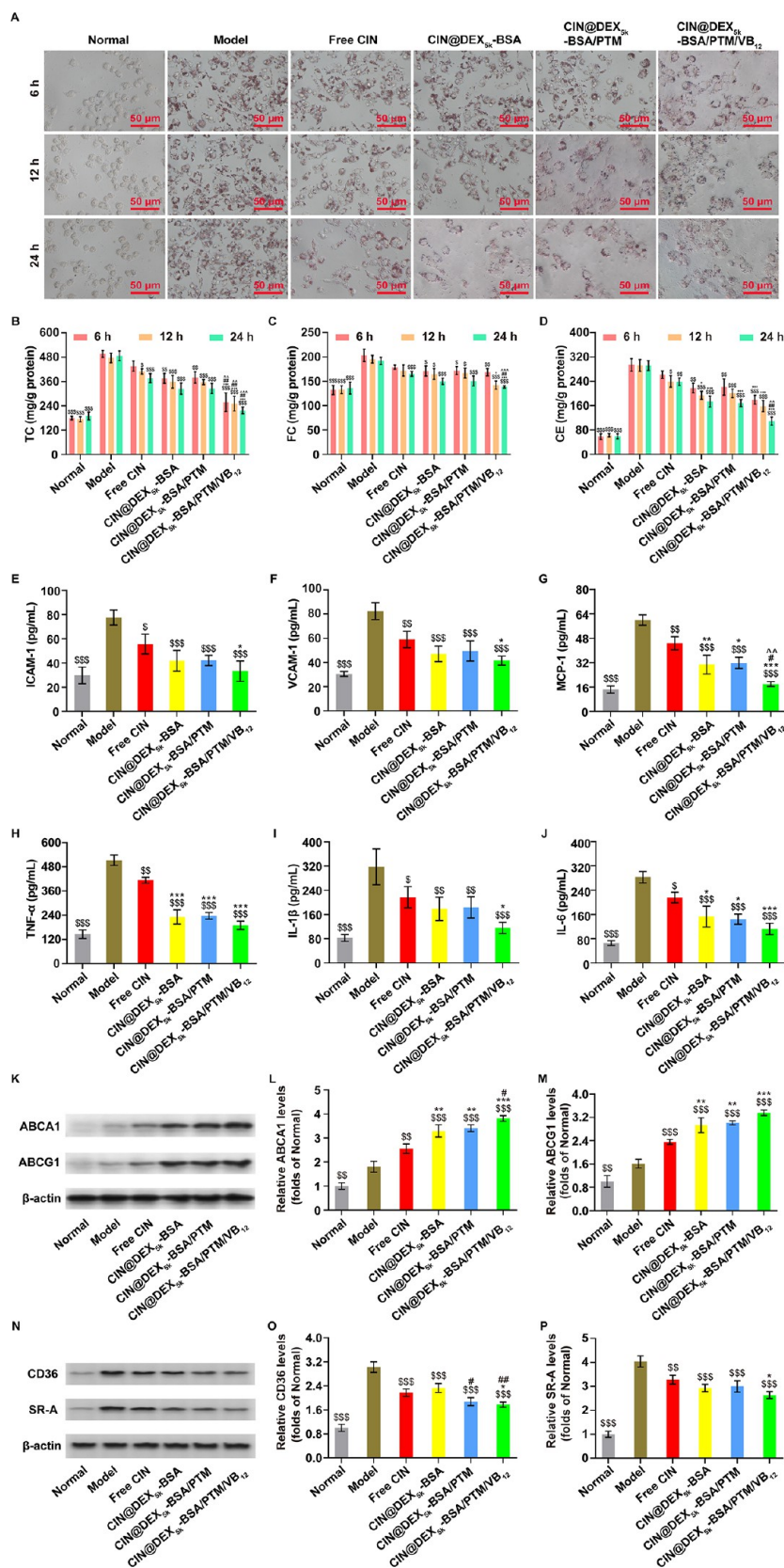


Figure 9. (A) Representative images of Oil Red O staining, scale bar 50 μm . (B–D) Intracellular levels of TC, FC, and CE. (E–J) Protein levels of ICAM-1, VCAM-1, MCP-1, TNF- α , IL-1 β , and IL-6 in THP-FMs. (K–P) Protein levels of ABCA1, ABCG1, CD 36, and SR-A in THP-FMs. $^{\$}p < 0.05$, $^{\$\$}p < 0.01$, $^{$$$}p < 0.001$ compared with model group; $^{*}p < 0.05$, $^{**}p < 0.01$, $^{***}p < 0.001$ compared with free CIN group; $^{\#}p < 0.05$, $^{\#\#}p < 0.01$ compared with CIN@DEX_{sk}-BSA; $^{\wedge}p < 0.01$, $^{\wedge\wedge}p < 0.001$ compared with CIN@DEX_{sk}-BSA/PTM. Each bar represents the mean \pm SD ($n = 3$).

have been reported as targeting ligands of scavenger receptor class A (SR-A), which is overexpressed on activated macrophages in the atherosclerotic region.^{52–54} Furthermore, the difference between the three DiR nanoemulsions accumulated in plaques may result from different oral bioavailability *in vivo*. It was supposed that VB₁₂ improved the permeability of CIN across the small intestine epithelium and DEX facilitated plaque accumulation. DiR@DEX_{5k}-BSA/PTM and DiR@DEX_{5k}-BSA/PTM/VB₁₂ respectively showed 5.28- and 6.25-fold increments in fluorescence signal at the aortic tree compared with that of the free DiR group. This indicates that @DEX_{5k}-BSA/PTM/VB₁₂ may have great potential to target atherosclerotic plaques after oral administration.

Therapeutic Effects of CIN-Loaded Nanoemulsions on AS. To assess the therapeutic effects of CIN, an AS mouse model was established using ApoE^{-/-} mice on a high-fat diet for 8 weeks. CIN preparations were orally administrated at an equivalent CIN dose of 50 mg/kg once a day for 8 weeks, while the normal group was fed with standard rodent feed and water (Figure 7A). Besides, Active Ingredient (SVT) was used as a positive control. After treatment, the formation of atherosclerotic plaques at the aortic arch was observed *in vivo* and the whole aortic tree was stained with Oil Red O *in vitro* for further evaluation (Figure 7B,C). Large white plaques were found in the model group, whereas these lesions were rarely seen in the SVT group. CIN preparations inhibited the formation of plaques and CIN@DEX_{5k}-BSA/PTM/VB₁₂ obtained similar amelioration effects on AS compared with those of SVT. The Oil Red O staining of the aortic tree demonstrated that the plaque area in the free SVT, free CIN, CIN@DEX_{5k}-BSA, CIN@DEX_{5k}-BSA/PTM, and CIN@DEX_{5k}-BSA/PTM/VB₁₂ groups were 11.3%, 19.09%, 15.89%, 12.13%, and 7.67%, respectively (Figure 7H). Furthermore, hematoxylin and eosin (HE) staining (Figure 7D,I), Oil Red O staining (Figure 7E,J), and Sirius red staining (Figure 7F,K) of the aortic roots were performed and quantified. Model mice had substantial plaques on the vascular surface, as indicated by extensive Oil Red O staining. A smooth artery wall with reduced plaque, fatty lines, and foam cells was observed in the SVT group, which was similar to that in the normal mice. Free CIN exhibited a slightly decreased Oil Red O staining area of the aortic roots. The therapeutic effect of CIN on AS was improved by administration with nanoemulsions, especially for CIN@DEX_{5k}-BSA/PTM/VB₁₂ in the plaque areas.

The body weight changes of mice were recorded during the treatment (Figure 7G). CIN nanoemulsions effectively controlled the weight gain of mice compared with that of the model group. The weight gain of mice in the CIN@DEX_{5k}-BSA/PTM/VB₁₂ group was similar to that of the SVT group. Atherosclerotic plaque formation was associated with hypercholesterolemia, and blood lipid levels were therefore measured at the end of the experiment. Model mice exhibited high levels of total cholesterol (TC), triglyceride (TG), and low-density lipoprotein cholesterol (LDL-C), and low levels of high-density lipoprotein cholesterol (HDL-C) and HDL-C/LDL-C. Administration of CIN preparations decreased the TC, TG, and LDL-C levels while increasing the HDL-C level and HDL-C/LDL-C ratio compared with those in the model group, especially for the CIN@DEX_{5k}-BSA/PTM/VB₁₂ group (Figure 7L–P). The enhancement of serum TC levels may predispose patients to hypercholesterolemia, which accelerates the development of AS.⁵⁵ The levels of TC in the SVT, free CIN, CIN@DEX_{5k}-BSA, CIN@DEX_{5k}-BSA/PTM, and CIN@

DEX_{5k}-BSA/PTM/VB₁₂ groups were 1.58-fold, 2.93-fold, 2.72-fold, 1.76-fold, and 1.46-fold that of the normal group, respectively. The high HDL-C/LDL-C ratios is a characteristic of a low risk of atherosclerotic disease and a low incidence of coronary deaths. The HDL-C/LDL-C ratio in the SVT, free CIN, CIN@DEX_{5k}-BSA, CIN@DEX_{5k}-BSA/PTM, and CIN@DEX_{5k}-BSA/PTM/VB₁₂ groups were 81.57%, 26.93%, 35.23%, 48.26%, and 58.38% compared with those in the normal group, respectively. Furthermore, no side effects were found in the safety evaluation (Figure S6). It is suggested that the increased oral bioavailability and plaque accumulation of CIN@DEX_{5k}-BSA/PTM/VB₁₂ may contribute to the enhanced therapeutic effects.

Therapeutic Mechanisms of CIN in Preventing the Progression of AS. Further studies were implemented to discover the mechanisms of CIN in the treatment of AS. The serum levels of atherosclerotic mediators, including intercellular adhesion molecule 1 (ICAM-1), vascular cell adhesion molecule 1 (VCAM-1), and monocyte chemoattractant protein-1 (MCP-1) were measured (Figure 8A–C). The levels of atherosclerotic mediators were significantly higher in model mice than those in normal mice, whereas these decreased following treatment with SVT or CIN preparations for 8 weeks. Among all CIN preparations, CIN@DEX_{5k}-BSA/PTM/VB₁₂ possessed comparative effects with SVT for the downregulation of AS-related factors in the serum. Given that the anti-inflammatory activities of CIN have been generally reported, the level of pro-inflammatory cytokines in serum was measured after treatment (Figure 8D–F). Levels of tumor necrosis factor alpha (TNF- α), interleukin 1 β (IL-1 β), and interleukin 6 (IL-6) in the model group were significantly higher than those in the normal mice. SVT and CIN preparations downregulated the secretion of pro-inflammatory cytokines.

As shown in previous studies, an increased HDL-C/LDL-C ratio may indicate a halt or delay in the progression of AS *via* reversing cholesterol transportation. CIN may exert its therapeutic effects on AS *via* regulating cholesterol transportation. The expression of transporters on macrophages that are closely related to the intake (CD36 and SR-A) and efflux (ABCA1 and ABCG1) of cholesterol were investigated using immunofluorescence (Figure 8G) and Western blotting (Figure 8H–M). CIN preparations significantly upregulated the expression of ABCA1 and ABCG1. The model group exhibited an increased expression of CD36 and SR-A, whereas both SVT and CIN preparations downregulated the expression of CD36 and SR-A to different degrees. Overall, CIN@DEX_{5k}-BSA/PTM/VB₁₂ significantly affected the increased expression of ABCA1 and ABCG1 and the decreased expression of CD36 and SR-A.

To validate the therapeutic mechanisms of CIN in AS, a foam cell model, THP-1 macrophage-derived foam cells (THP-FM), was established *in vitro*. Free CIN and CIN nanoemulsions exhibited no cytotoxicity on the differentiation of monocytes into macrophages (THP-MS) with 0.5–24 μ g/mL of CIN (Figure S7). Oil Red O staining showed that free CIN treatment reduced lipid droplet accumulation in THP-FM cells, and no significant difference was observed among the CIN nanoemulsion groups (Figure 9A). CIN preparations reduced the intracellular cholesterol level as indicated by the levels of TC, free cholesterol (FC), and cholesterol ester (CE) in the THP-FM cells (Figure 9B–D). The levels of atherosclerotic mediators (ICAM-1, VCAM-1, and MCP-1)

and pro-inflammatory cytokines (TNF- α , IL-1 β , and IL-6) secreted by THP-FM cells were also measured (Figure 9E–J). CIN preparations downregulated the level of pro-inflammatory cytokines and atherosclerotic mediators, especially for CIN@DEX_{5k}-BSA/PTM/VB₁₂. In agreement with the *in vivo* study, CIN preparations significantly upregulated the expression of ABCA1 and ABCG1 and downregulated that of CD36 and SR-A in THP-FM cells (Figure 9K–P). Collectively, the mechanisms of CIN in preventing the progression of AS may be attributed to its anti-inflammatory activity and inhibitory effects on intracellular cholesterol accumulation by regulating the expression of transporters.

Statin drugs have been a cornerstone in the clinical management of hyperlipidemia and reducing the risk of atherosclerotic cardiovascular disease by decreasing the level of LDL-C. Nonetheless, the safety of statin drugs remains a major concern because of their adverse effects, such as hepatotoxicity and myopathy, highlighting the need for nontraditional therapeutic drugs.^{56,57} Plant-derived essential oils have multi-targeted and pleiotropic pharmacological properties because of their interactions with various cell types and intracellular molecular pathways involved in atherogenesis. However, the low oral bioavailability and high volatility of essential oils require ODDS to achieve pharmacological actions *in vivo*.^{8,9} Numerous nanocarriers have been developed to facilitate the oral delivery of essential oils, including various nano-emulsions,¹⁴ Pickering emulsions,⁵⁸ inclusion compounds⁵⁹ and solid lipid nanoparticles.⁶⁰ However, limited studies indicated a comprehensive strategy for encapsulating essential oils in the interior region of nanocarriers without content loss and consolidating the outer layer of nanocarriers to prevent volatilization. We developed microjet-based nanoemulsion preparation techniques to encapsulate CIN into the oil phase without content loss by using temperatures below the boiling point of CIN. Moreover, an optimal protein/protein–polysaccharide emulsifier and a UV irradiation-mediated protein gelation method were developed to reinforce the surface of emulsion droplets, which improved the stability of CIN both *in vitro* and *in vivo*. Furthermore, targeting the delivery of essential oils to atherosclerotic regions after oral absorption was enabled by these protein–polysaccharide based nanoemulsions. Therefore, we developed an ODDS for effective preparation, improved oral absorption, and targeted delivery of essential oils.

STUDY LIMITATIONS

Although the nanoemulsions developed for oral administration of essential oils based on a polysaccharide-protein/protein complex improved the bioavailability of CIN and exhibited attractive therapeutic effects on AS, this process (developed in this study) has some limitations. This study demonstrated that CIN@DEX_{5k}-BSA/PTM/VB₁₂ at the dose of 50 mg/kg/day alleviated atherosclerotic lesions after oral administration for 8 weeks. However, whether CIN@DEX_{5k}-BSA/PTM/VB₁₂ at the same dosage is still effective or safe after a longer-term administration (for example, 24 weeks) remains unknown. This problem should be solved in the future. Furthermore, the therapeutic effects of CIN and its nanoemulsions were restricted to the atherosclerotic ApoE^{-/-} mouse model at an early stage of AS. Therefore, further validation of the AS model in the middle and advanced stages with long-term medication is necessary for the comprehensive evaluation of

the anti-AS effects of CIN and CIN@DEX_{5k}-BSA/PTM/VB₁₂ nanoemulsion.

CONCLUSION

Herein, we developed a polysaccharide-protein/protein complex emulsifier comprising BSA-DEX, PTM, and VB₁₂ to formulate an oral nanoemulsion for an essential oil-CIN. A microjet method followed by UV treatment was exploited to prepare the nanoemulsion, which exhibited good temperature control from beginning to end. CIN@DEX_{5k}-BSA/PTM/VB₁₂ considerably improved the stability of CIN both *in vivo* and *in vitro*, promoted permeability across the Caco-2 cell monolayer and mucus, and enhanced the bioavailability and plaque accumulation of CIN. It was demonstrated that CIN and its formulations played a role in combating AS through anti-inflammatory activity and inhibition of intracellular cholesterol accumulation. This work highlights CIN as a valuable candidate for AS treatment and provides a promising oral formulation of essential oils to facilitate their clinical application.

METHODS

Preparation of DEX-BSAs. The DEX-BSAs were prepared by the Maillard reaction.⁶¹ The BSA and DEXs (5, 10, and 20 kDa) were respectively dissolved in deionized water and then adjusted to pH 6, 7, and 8. After 12 h, the reaction solution was freeze-dried, and the freeze-dried powder was placed in a closed container containing saturated KBr at 60 °C for 24 h. The molecular weight distributions of DEX_{5k}-BSA, DEX_{10k}-BSA, and DEX_{20k}-BSA were analyzed by sodium dodecyl sulfate polyacrylamide gel electrophoresis (SDS-PAGE). After staining the gel with Coomassie brilliant blue, the SDS-PAGE patterns of DEX-BSAs were obtained. The conjugation degrees of the conjugates were determined by the OPA method (described in the Supporting Information). The DEX-BSAs were respectively used to prepare nanoemulsions and loaded with NR (NR@DEX-BSA) (described in the Supporting Information). The leakage rate of NR was determined by the super centrifugation method to screen the most stable nanoemulsion material (described in the Supporting Information).

Preparation of CIN@DEX_{5k}-BSA. The DEX_{5k}-BSA was weighted and dissolved in deionized water at 10 mg/mL. Then, the DEX_{5k}-BSA was mixed with 1 mL of CIN/MCT (1:4, v/v) solution at the oil–water volume ratio of 1:4. The resultant solution was vortexed and followed with sonication in an ice–water bath to obtain a primary emulsion. Subsequently, the primary emulsion was homogenized by a microjet high pressure homogenizer (NanoGenizer 20K, Genizer LLC, Los Angeles, USA) at a pressure of 6000 psi for 3 cycles. The post-treatment was carried out by heating at 90 °C or irradiation with a UV lamp (253.7 nm, Philips Electronics Ltd., Amsterdam, Netherlands). The structural changes of blank nanoemulsion (@DEX_{5k}-BSA) after heating or UV irradiation were detected by SDS-PAGE. After irradiation, the thermographic maps and temperature of CIN-loaded nanoemulsions were recorded by an infrared thermal imaging camera at different times. The drug content changes of CIN@DEX_{5k}-BSAs were also quantitatively analyzed by high-performance liquid chromatography (HPLC) with a UV detector (LC-16, Shimadzu Instruments Co., Ltd., Kyoto, Japan). For the detection of CIN, a mobile phase of acetonitrile/water (56:44, v/v) was used and detected at $\lambda = 203$ nm. Besides, the drug release of NR@DEX_{5k}-BSA in artificial gastrointestinal fluid (GIF) was investigated (described in the Supporting Information).

Preparation of CIN@DEX_{5k}-BSA/PTM. DEX_{5k}-BSA was mixed with PTM at a molar ratio of PTM-to-BSA 0.8:1, 1.6:1 and 3.2:1, and the pH of the mixture (DEX_{5k}-BSA/PTM) was adjusted from 2 to 9. The DEX_{5k}-BSA/PTM solutions were used to prepare blank nanoemulsions (@DEX_{5k}-BSA/PTMs). The ZP of the @DEX_{5k}-BSA/PTMs was determined by a dynamic laser scattering (DLS)

instrument (90Plus PALS, Brookhaven Instruments Co., Ltd., USA) to select the optimal pH reaction condition. In addition, the @DEX_{5k}-BSA/PTM-FITC was prepared by using fluorescence-labeled PTM-FITC at pH 7. Part of the @DEX_{5k}-BSA/PTM-FITC was irradiated by a UV lamp at 36 W for 90 min. Then, unbound PTM-FITC was separated by ultrafiltration at 4000 rpm for 3 min. The FL of unbound PTM-FITC (I_1) and total PTM-FITC (I_0) were determined by a fluorescence spectrophotometer (Cary Eclipse, Varian Technology Inc., California, USA), and the unbound ratio (I_1/I_0) of PTM-FITC was calculated. The stability of the @DEX_{5k}-BSA/PTMs was evaluated by monitoring the PDI changes for 28 days at 4 °C by DLS. The drug release of NR-loaded nanoemulsion (NR@DEX_{5k}-BSA/PTM) in artificial GIF was investigated. The structure of @DEX_{5k}-BSA/PTM was characterized by DSC and thermogravimetric analysis with a simultaneous thermal analyzer (STA 449F3, Netzsch Instruments Co., Ltd., Selb, Germany), and by FT-IR with an infrared spectral spectrometer (IS50, Thermo Fisher Scientific Inc., PA, USA). Meanwhile, the protein/protein-polysaccharide compound (DEX_{5k}-BSA/PTM), the physical mixture (DEX_{5k}-BSA+PTM), materials of PTM or DEX_{5k}-BSA were also detected. DEX_{5k}-BSA/PTM with a PTM-to-BSA solutions molar ratio of 1.6:1 was then used to prepare CIN-loaded nanoemulsions. The morphology of CIN-loaded nanoemulsions under different preparation conditions was observed using a TEM (H-7800, Hitachi Co., Ltd., Tokyo, Japan).

Preparation of CIN@DEX_{5k}-BSA/PTM/VB₁₂. The CIN@DEX_{5k}-BSA/PTM was prepared according to the optimal conditions above. Before UV irradiation, VB₁₂ solution was added to the emulsion with a VB₁₂-to-BSA molar ratio of 0.5:1, 0.75:1, 1:1 and stirred at 100 rpm for 12 h. Then, the CIN@DEX_{5k}-BSA/PTM/VB₁₂ was obtained by irradiation with a UV lamp. The binding efficiency of VB₁₂ on the CIN@DEX_{5k}-BSA/PTM/VB₁₂ was determined (described in the Supporting Information). The PS, PDI, and ZP of the prepared preparations were measured by the DLS method. Then, the CIN-loaded nanoemulsions were prepared. The concentration of VB₁₂ was optimized by evaluating the ability of CIN@DEX_{5k}-BSA/PTM/VB₁₂ to cross the mucus layer and Caco-2 cell monolayer (described in the Supporting Information). Besides, the surface composition of CIN@DEX_{5k}-BSA/PTM/VB₁₂ was studied (described in the Supporting Information) by an XPS (AXIS, Shimadzu Instruments Co., Ltd., Kyoto, Japan).

Characterization of CIN@DEX_{5k}-BSA/PTM/VB₁₂. CIN@DEX_{5k}-BSA/PTM/VB₁₂ was prepared under optimal conditions. In short, DEX_{5k}-BSA and PTM were mixed at a molar ratio of PTM-to-BSA 1.6:1. The resultant solution was adjusted to pH 7 and vortexed. Then, 4 mL of the DEX_{5k}-BSA/PTM mixture solution was mixed with 1 mL of the CIN/MCT solution. The resultant solution was sonicated and homogenized. Subsequently, VB₁₂ solution was finally added to the emulsion with a VB₁₂-to-BSA molar ratio of 0.75:1. The CIN@DEX_{5k}-BSA/PTM/VB₁₂ was obtained by irradiation with a UV lamp. Unloaded CIN was separated from emulsions using a Sephadex G-50 column. The PS, PDI, and ZP of the prepared preparations were measured. The LE and LC were calculated. The release of CIN from CIN@DEX_{5k}-BSA, CIN@DEX_{5k}-BSA/PTM, and CIN@DEX_{5k}-BSA/PTM/VB₁₂ in the artificial GIF was investigated (described in the Supporting Information). The changes of PS, PDI, ZP, and remaining concentration of CIN in nanoemulsions within 90 days were monitored at 4 °C.

Transcellular Permeation Assessment on the Caco-2 Cell Monolayer. Caco-2 cells were utilized as a model of gastrointestinal epithelium *in vitro*. Caco-2 cells (5×10^4 cells/well) were seeded in transwell plates (pore size 0.4 μm). After the TEER values reached 500 Ω·cm², cell monolayers were used in the following experiment. First, mucin was added into the apical medium at 10 mg/mL to simulate the presence of mucus, while mucin-free medium was used to simulate the mucus-deprived condition. Then, 20 μL of IF (100 IU/mL) and 0.2 mL of CIN preparations (10 mg/mL CIN) were respectively added in the upper chambers. At 2 h, parts of the apical and basolateral medium were respectively collected and observed under a TEM. In addition, part of the basolateral medium was withdrawn and analyzed by the HPLC for the content of CIN. The

P_{app} of CIN was calculated (described in the Supporting Information). For the study of intracellular uptake, the cells were harvested and repeatedly freeze-thawed and lysed for 1 h. The cellular uptake of CIN was determined by HPLC. Besides, TEER values were measured to monitor the impact of CIN preparations on the monolayer integrity. The initial TEER values of the Caco-2 cell monolayer were determined. After that, the apical media were removed and replaced with 0.2 mL of CIN preparations (10 mg/mL CIN). At 2 h, the CIN preparations were withdrawn from the upper chambers and replaced with PBS. The TEER values of the Caco-2 cell monolayer in different groups were measured. Lastly, to investigate the related cellular internalization mechanism of CIN preparations, Caco-2 cell monolayer were first preincubated for 30 min with different specific endocytotic inhibitors and then treated with IF (20 μL, 100 IU/mL) and CIN preparations (0.2 mL, 10 mg/mL CIN) for 2 h. The P_{app} values of CIN were calculated.

The Stability of @DEX_{5k}-BSA/PTM/VB₁₂ in Various Simulated Media. To investigate the degradation of @DEX_{5k}-BSA/PTM/VB₁₂ in SGF and SIF, FRET analysis was performed. The HIQ and NR (FRET pairs) coloaded nanoemulsions were prepared (described in the Supporting Information) and mixed with SGF or SIF in tubes. After incubating in a 37 °C thermostatic shaking bed for different times, samples were taken from the tubes and loaded onto a 96-well plate. Then, the fluorescence images of each well were acquired through an IVIS (IVIS, Luminal III, Caliper, USA). The FL was measured through a fluorescence spectrophotometer with excitation and emission wavelengths set at 510 and 635 nm, respectively. The FRET ratio was calculated using the following equation, where I_{HIQ} and I_{NR} were the fluorescence intensities of HIQ and NR at 510 and 635 nm, using an excitation wavelength of 450 nm, respectively.

$$\text{FRET ratio} = \frac{I_{NR}}{I_{NR} + I_{HIQ}}$$

Distribution of @DEX_{5k}-BSA/PTM/VB₁₂ in the GIT. The C57BL/6J mice were divided into four groups and fasted for 12 h with free access to water. To perform imaging, DiR-loaded nanoemulsions were prepared. Then, free DiR, DiR@DEX_{5k}-BSA, DiR@DEX_{5k}-BSA/PTM or DiR@DEX_{5k}-BSA/PTM/VB₁₂ were respectively orally administrated at the dose of 2 mg/kg DiR. The mice were sacrificed at 0.5, 2, 6, and 12 h postadministration. The stomachs and intestines were isolated from mice and DiR distribution was detected with IVIS. Besides, parts of mice were sacrificed at 0.5, 2, 6, and 12 h postadministration, and the small intestinal tissue was taken out, opened and gently washed with saline. Transverse sections of the ileum were obtained, stained with DAPI, and visualized using a confocal microscope (FV1000, Olympus Co., Ltd., MN, USA).

Pharmacokinetics Study. The C57BL/6J mice were divided into 4 groups randomly, and treated with free CIN, CIN@DEX_{5k}-BSA, CIN@DEX_{5k}-BSA/PTM, or CIN@DEX_{5k}-BSA/PTM/VB₁₂ at a dose of 50 mg/kg CIN *via* oral gavage. At different time points, mice in each group were anesthetized with inhaled Active Ingredient Then the blood was sampled from the aortavertralis and detected as in previous reports.⁴⁶ After centrifugation, 100 μL plasma was mixed with 20 μL butyl acetate and 380 μL cyclohexane. The mixture was centrifuged at 5000 rpm for 10 min at 4 °C and the supernatant from each aliquot (1 μL) was injected into the GC-MS system for assay. The GC-MS analysis was performed with a GC-MS-TQ8050NX (Shimadzu Instruments Co., Ltd., Kyoto, Japan) equipped with an SH-Stabilwax column (30 m × 0.25 μm × 0.32 mm capillary column chemically bonded with cross-bond carbowax polyethylene glycol, Shimadzu Instruments Co., Ltd., Kyoto, Japan). The pharmacokinetic data were analyzed by the pharmacokinetic software WinNonlin 8.3 (Pharsight, Mountain View, CA, USA).

Assessment of the Targeting Capability to Atherosclerotic Lesions. The 8-week-old ApoE^{-/-} mice were fed with a western diet containing 21% fat and 0.15% cholesterol for 8 weeks to obtain atherosclerotic mice. The model mice were randomized into 4 groups and treated with free DiR, DiR@DEX_{5k}-BSA, DiR@DEX_{5k}-BSA/PTM or DiR@DEX_{5k}-BSA/PTM/VB₁₂ at a DiR dose of 2 mg/kg by

gavage. At 12 h after gavage, all animals were subjected to euthanasia, and hearts, livers, spleens, lungs, kidneys, and aortic trees were entirely dissected. After appropriate disposal, the images for tissues and aortic trees were taken by IVIS and analyzed by the Living Image 4.4.

Animal Grouping and Treatments. ApoE^{-/-} mice on a C57BL/6J background were randomized into 7 groups and named: normal, model, free SVT, free CIN, CIN@DEX_{sk}-BSA, CIN@DEX_{sk}-BSA/PTM, and CIN@DEX_{sk}-BSA/PTM/VB₁₂ groups. Mice in the normal group were fed with standard rodent food and water during the periods of the experiment. Mice in the other six groups were fed with western diet containing 21% fat and 0.15% cholesterol. After 8 weeks of modeling, each group was treated for 8 weeks. Mice in the free SVT were intragastrically administered with the lipid-lowering drug SVT at a dose of 2.5 mg/kg/day. All the CIN preparation groups were treated at a CIN dose of 50 mg/kg/day. The body weights of mice were recorded during the course of treatment. After that, all the mice were sacrificed, and the blood, aortic trees, and organs were collected.

Evaluation of En Face Lesion Area. After euthanasia, the whole aortic tree and tissues of ApoE^{-/-} mice were dissected. The aortic tree was then stained with Oil Red O and photographed. The percentage of lesion area stained by Oil Red O in the aortic surface was studied by ImageJ 1.8.0.

Assessment of Atherosclerotic Lesions. The sections of the aortic root were subjected to HE staining, Oil Red O, and Sirius red staining to evaluate plaque area, lipid deposition and collagen content, respectively. Quantitative analyses were conducted by means of ImageJ 1.8.0.

Immunofluorescence. Glycine-quenched and formalin-fixed cross sections of the aortic root were permeabilized using 0.5% saponin in PBS. Nonspecific labeling was blocked with 10% goat serum with 0.1% Saponin in PBS for 2 h. Sections of aortic root were incubated with rabbit monoclonal antibody against ABCA1 (1:100), rabbit monoclonal antibody against ABCG1 (1:100), rabbit monoclonal antibody against CD36 (1:100) or mouse monoclonal antibody against SR-A (1:50) overnight at 4 °C. After washing with 0.1% Saponin SSC, sections were incubated in antibody buffer containing mouse antirabbit IgG-FITC antibody (1:100) or m-IgGκ BP-FITC (1:50) for 2 h at RT. After washing with 0.1% Saponin SSC, the nuclei were stained by DAPI. Images were taken by a confocal laser scanning microscope.

Measurement of Serum Lipid Levels. Blood samples from the mice were collected and added into tubes. Serum levels of TC, TG, HDL-C, and LDL-C were measured by enzymatic methods using commercial kits.

Western Blot Analysis. The aortas of mice were lysed with the RIPA lysis buffer containing 0.1 mmol/L PMSF on ice, and total proteins were isolated and measured with a BCA Assay Kit. Then, the protein extracts were subjected to SDS-PAGE and transferred to a polyvinylidene difluoride (PVDF) membrane. After adding 5% skim milk, the membranes were then immunoblotted with rabbit anti-ABCA1 (1:500), rabbit anti-ABCG1 (1:1000), rabbit anti-CD36 (1:500), mouse anti-SR-A (1:1000) with gentle shaking at 4 °C for 12 h. After repeated rinses with PBST, the membranes were incubated with HRP-conjugated Goat Anti-Rabbit IgG secondary antibodies (1:10000) and Rabbit Anti-Mouse IgG secondary antibodies (1:10000). The protein bands were visualized using ECL solution and analyzed utilizing Gel-Pro software 4.0.

Evaluation of Atherosclerotic Mediators and Inflammatory Cytokines in Serum. Concentrations of ICAM-1, VCAM-1, MCP-1, TNF- α , IL-1 β , and IL-6 in serum were quantified with the enzyme-linked immunosorbent assay using commercial kits following the manufacturer's instructions.

Cell Culture and Treatment. To stimulate the differentiation of monocytes into macrophages (THP-MS), THP-1 cells were treated with 160 nM PMA for 24 h. THP-MS were then incubated with 50 μ g/mL ox-LDL for 48 h to transform into foam cells. Then, the DMEM medium of THP-1 macrophage-derived foam cells (THP-FM) was removed and equilibrated with prewarmed free CIN, CIN@

DEX_{sk}-BSA, CIN@DEX_{sk}-BSA/PTM or CIN@DEX_{sk}-BSA/PTM/VB₁₂ (20 μ g/mL CIN) for different times. Meanwhile, THP-MS cells were used as the normal group and THP-FM was used as the model group. The cytotoxicity of CIN preparations on THP-MS cells was measured (described in the Supporting Information).

Evaluation of Intracellular Lipid Droplets by Oil Red O Staining. After treatment, THP-FM cells were washed and fixed in 4% paraformaldehyde for 5 min. After repeated rinses, THP-FM cells were stained with the Oil Red O working solution at 37 °C in the dark, and further destained with 60% isopropanol. Finally, the photos of Oil Red O-positive cells were acquired by the inverted microscope (ECLIPSE Ti2, NIKON Instrument Inc., Tokyo, Japan).

Detection of Intracellular Cholesterol. After treatment, THP-FM cells were broken in 1 mL 0.9% NaCl using an ultrasonic cell disrupter under an ice bath. Following centrifugation (12,000 rpm, 5 min), the supernatant was evenly divided into two parts, one part was used to determine the protein content by the BCA method, and the other part was added with an equal volume of mixture solvent (chloroform:methanol = 2:1, v/v). The mixture was vortexed for 5 min and centrifuged at 1500 rpm for 5 min at 15 °C. Then, the upper organic phase was collected and dried with nitrogen in a desiccator at 60 °C to remove the organic solvent. Add 500 μ L of absolute ethanol, the TC, FC, and CE were detected using the cholesterol oxidase method for automatic biochemical analysis.

Western Blot Analysis. After 24 h treatment, the THP-FM cells were lysed and centrifuged. The concentration of protein extracts was quantified by a BCA protein assay kit. Protein lysates were subjected to a 10% SDS-PAGE and transferred to PVDF membranes. Membranes were blocked by 5% skim milk and incubated overnight with primary antibodies at 4 °C. After that, membranes were washed and incubated with the secondary antibodies. Then, the protein bands were visualized and analyzed.

Detection of Atherosclerotic Mediators and Inflammatory Cytokines. After 24 h treatment, supernatants from treated THP-FM cells of different groups were assessed for ICAM-1, VCAM-1, MCP-1, TNF- α , IL-1 β , and IL-6 by the enzyme-linked immunosorbent assay using commercial kits following the instructions.

Statistical Analysis. Results were exhibited in the form of mean \pm standard deviation. One-way ANOVA analysis with a *post hoc* Tukey–Kramer test was used for statistical comparison among groups by the GraphPad Prism 9.0 software. The *p* value less than 0.05 was identified as statistically significant.

ASSOCIATED CONTENT

Supporting Information

The Supporting Information is available free of charge at <https://pubs.acs.org/doi/10.1021/acsnano.2c12230>.

Additional methods and detailed experimental procedures; physicochemical properties of NR-loaded nanoemulsions in Table S1; binding efficiency of VB₁₂ in Table S2; XPS spectra analysis of surface elements in Table S3; characteristics of various nanoemulsions in Tables S4–S5; material properties of DEX-BSAs in Figure S1; UV absorption curve in Figure S2; the appearance of various nanoemulsions in Figure S3; PS and PDI of nanoemulsions in the apical and basolateral medium in Figure S4; FRET ratio of nanoemulsions prepared with HIQ and NR in Figure S5; safety evaluation in Figures S6–S7 (PDF)

AUTHOR INFORMATION

Corresponding Authors

Qianming Du – General Clinical Research Center of Nanjing First Hospital, Nanjing Medical University, Nanjing 210006, China; School of Basic Medicine & Clinical Pharmacy, China

Pharmaceutical University, Nanjing 210009, China;
Email: duqianming@njmu.edu.cn

Haiyu Xu – Institute of Chinese Materia Medica, China Academy of Chinese Medical Sciences, Beijing 100700, China; Email: hy_xu627@163.com

Zipeng Gong – State Key Laboratory of Functions and Applications of Medicinal Plants, Guizhou Provincial Key Laboratory of Pharmaceutics, and School of Pharmaceutical Sciences, Guizhou Medical University, Guiyang 550025, China; orcid.org/0000-0003-2074-9476;
Email: gzp4012607@126.com

Authors

Yi Chen – State Key Laboratory of Functions and Applications of Medicinal Plants and School of Pharmaceutical Sciences, Guizhou Medical University, Guiyang 550025, China

Jianing Wang – Department of Pharmacy of the Affiliated Jiangning Hospital, Nanjing Medical University, Nanjing 210006, China

Jinzhuang Xu – State Key Laboratory of Functions and Applications of Medicinal Plants and School of Pharmaceutical Sciences, Guizhou Medical University, Guiyang 550025, China

Jiyuan Zhang – School of Pharmacy, China Pharmaceutical University, Nanjing 210009, China

Shan Xu – State Key Laboratory of Functions and Applications of Medicinal Plants and School of Pharmaceutical Sciences, Guizhou Medical University, Guiyang 550025, China

Qing Zhang – State Key Laboratory of Functions and Applications of Medicinal Plants, Guizhou Provincial Key Laboratory of Pharmaceutics, and School of Pharmaceutical Sciences, Guizhou Medical University, Guiyang 550025, China

Jing Huang – State Key Laboratory of Functions and Applications of Medicinal Plants and School of Pharmaceutical Sciences, Guizhou Medical University, Guiyang 550025, China

Jianqing Peng – State Key Laboratory of Functions and Applications of Medicinal Plants and School of Pharmaceutical Sciences, Guizhou Medical University, Guiyang 550025, China

Complete contact information is available at:

<https://pubs.acs.org/10.1021/acsnano.2c12230>

Author Contributions

[†]Y.C., J.W., and J.X. contributed equally to this work.

Notes

The authors declare no competing financial interest.

ACKNOWLEDGMENTS

This work was financially supported by the National Natural Science Foundation of China (82104537, 82172558); the Distinguished Young Scholars of Nanjing (JQX20008); the Excellent Young Talents Plan of Guizhou Medical University (2020-102, 2021-103, 2022-104); Doctor of Entrepreneurship and Innovation Funds of Jiangsu (JSSCBS20222019); the General Project of Nanjing Medical Science and Technology Development Fund (YKK22223).

REFERENCES

(1) Herrington, W.; Lacey, B.; Sherliker, P.; Armitage, J.; Lewington, S. Epidemiology of Atherosclerosis and the Potential to Reduce the

Global Burden of Atherothrombotic Disease. *Circ. Res.* **2016**, *118*, 535–546.

(2) Mohanta, S. K.; Peng, L.; Li, Y.; Lu, S.; Sun, T.; Carnevale, L.; Perrotta, M.; Ma, Z.; Forstera, B.; Stanic, K.; Zhang, C.; Zhang, X.; Szczepaniak, P.; Bianchini, M.; Saeed, B. R.; Carnevale, R.; Hu, D.; Nosalski, R.; Pallante, F.; Beer, M.; Santovito, D.; et al. Neuroimmune Cardiovascular Interfaces Control Atherosclerosis. *Nature* **2022**, *605*, 152–159.

(3) Swirski, F. K.; Nahrendorf, M. Leukocyte Behavior in Atherosclerosis, Myocardial Infarction, and Heart Failure. *Science* **2013**, *339*, 161–166.

(4) Yang, J.; Zhong, C.; Yu, J. Natural Monoterpenes As Potential Therapeutic Agents Against Atherosclerosis. *Int. J. Mol. Sci.* **2023**, *24*, 2429.

(5) Zhang, Y.; Gu, Y.; Chen, Y.; Huang, Z.; Li, M.; Jiang, W.; Chen, J.; Rao, W.; Luo, S.; Chen, Y.; Chen, J.; Li, L.; Jia, Y.; Liu, M.; Zhou, F. Dingxin Recipe Iv Attenuates Atherosclerosis by Regulating Lipid Metabolism Through LXR- α /SREBP1 Pathway and Modulating the Gut Microbiota in ApoE-/- Mice Fed with HFD. *J. Ethnopharmacol.* **2021**, *266*, 113436.

(6) Jiang, F.; Wu, G.; Li, W.; Yang, J.; Yan, J.; Wang, Y.; Yao, W.; Zhou, X.; He, Z.; Wu, L.; Xiao, C.; Xiao, T.; Zhang, M.; Shen, X.; Tao, L. Preparation and Protective Effects of 1,8-Cineole-Loaded Self-Microemulsifying Drug Delivery System on Lipopolysaccharide-Induced Endothelial Injury in Mice. *Eur. J. Pharm. Sci.* **2019**, *127*, 14–23.

(7) Linghu, K.; Lin, D.; Yang, H.; Xu, Y.; Zhang, Y.; Tao, L.; Chen, Y.; Shen, X. Ameliorating Effects of 1,8-Cineole on Lps-Induced Human Umbilical Vein Endothelial Cell Injury by Suppressing NF- κ B Signaling in Vitro. *Eur. J. Pharmacol.* **2016**, *789*, 195–201.

(8) Linghu, K. G.; Wu, G. P.; Fu, L. Y.; Yang, H.; Li, H. Z.; Chen, Y.; Yu, H.; Tao, L.; Shen, X. C. 1,8-Cineole Ameliorates Lps-Induced Vascular Endothelium Dysfunction in Mice Via PPAR- γ Dependent Regulation of NF- κ B. *Front. Pharmacol.* **2019**, *10*, 178.

(9) Peng, J.; Jiang, Z.; Wu, G.; Cai, Z.; Du, Q.; Tao, L.; Zhang, Y.; Chen, Y.; Shen, X. Improving Protection Effects of Eucalyptol Via Carboxymethyl Chitosan-Coated Lipid Nanoparticles on Hyperglycaemia-Induced Vascular Endothelial Injury in Rats. *J. Drug Targeting* **2021**, *29*, 520–530.

(10) Jun, H. J.; Hoang, M. H.; Yeo, S. K.; Jia, Y.; Lee, S. J. Induction of ABCA1 and ABCG1 Expression by the Liver X Receptor Modulator Cineole in Macrophages. *Bioorg. Med. Chem. Lett.* **2013**, *23*, 579–583.

(11) Li, J.; Chen, B.; Yu, T.; Guo, M.; Zhao, S.; Zhang, Y.; Jin, C.; Peng, X.; Zeng, J.; Yang, J.; Song, X. An Efficient Controlled Release Strategy for Hypertension Therapy: Folate-Mediated Lipid Nanoparticles for Oral Peptide Delivery. *Pharmacol. Res.* **2020**, *157*, 104796.

(12) Paul, K.; Bhattacharjee, P.; Chatterjee, N.; Pal, T. K. Nanoliposomes of Supercritical Carbon Dioxide Extract of Small Cardamom Seeds Redresses Type 2 Diabetes and Hypercholesterolemia. *Recent Pat. Biotechnol.* **2019**, *13*, 284–303.

(13) Lu, W.-C.; Huang, D.-W.; Wang, C.-C. R.; Yeh, C.-H.; Tsai, J.-C.; Huang, Y.-T.; Li, P.-H. Preparation, Characterization, and Antimicrobial Activity of Nanoemulsions Incorporating Citral Essential Oil. *J. Food Drug Anal.* **2018**, *26*, 82–89.

(14) Bashlouei, S. G.; Karimi, E.; Zareian, M.; Oskoueian, E.; Shakeri, M. Heracleum Persicum Essential Oil Nanoemulsion: a Nanocarrier System for the Delivery of Promising Anticancer and Antioxidant Bioactive Agents. *Antioxidants (Basel)* **2022**, *11*, 831.

(15) Liu, Q.; Gao, Y.; Fu, X.; Chen, W.; Yang, J.; Chen, Z.; Wang, Z.; Zhuansun, X.; Feng, J.; Chen, Y. Preparation of Peppermint Oil Nanoemulsions: Investigation of Stability, Antibacterial Mechanism and Apoptosis Effects. *Colloids Surf., B* **2021**, *201*, 111626.

(16) Banasaz, S.; Morozova, K.; Ferrentino, G.; Scampicchio, M. Encapsulation of Lipid-Soluble Bioactives by Nanoemulsions. *Molecules* **2020**, *25*, 3966.

- (17) Huang, K.; Liu, R.; Zhang, Y.; Guan, X. Characteristics of Two Cedarwood Essential Oil Emulsions and Their Antioxidant and Antibacterial Activities. *Food Chem.* **2021**, *346*, 128970.
- (18) Tarhan, O.; Spotti, M. J. Nutraceutical Delivery Through Nanoemulsions: General Aspects, Recent Applications and Patented Inventions. *Colloids Surf., B* **2021**, *200*, 111526.
- (19) Qi, J.; Huang, C.; He, F.; Yao, P. Heat-Treated Emulsions with Cross-Linking Bovine Serum Albumin Interfacial Films and Different Dextran Surfaces: Effect of Active Ingredient Delivery. *J. Pharm. Sci.* **2013**, *102*, 1307–1317.
- (20) Rajasekaran, B.; Singh, A.; Benjakul, S. Combined Effect of Chitosan and Bovine Serum Albumin/Whey Protein Isolate on the Characteristics and Stability of Shrimp Oil-in-Water Emulsion. *J. Food Sci.* **2022**, *87*, 2879–2893.
- (21) Guo, Y.; Huang, W. C.; Wu, Y.; Qi, X.; Mao, X. Conformational Changes of Proteins and Oil Molecules in Fish Oil/Water Interfaces of Fish Oil-in-Water Emulsions Stabilized by Bovine Serum Albumin. *Food Chem.* **2019**, *274*, 402–406.
- (22) Dickinson, E. Milk Protein Interfacial Layers and the Relationship to Emulsion Stability and Rheology. *Colloids Surf., B* **2001**, *20*, 197–210.
- (23) Aguilera-Garrido, A.; Del Castillo-Santaella, T.; Yang, Y.; Galisteo-Gonzalez, F.; Galvez-Ruiz, M. J.; Molina-Bolivar, J. A.; Holgado-Terriza, J. A.; Cabrerizo-Vilchez, M. A.; Maldonado-Valderrama, J. Applications of Serum Albumins in Delivery Systems: Differences in Interfacial Behaviour and Interacting Abilities with Polysaccharides. *Adv. Colloid Interface Sci.* **2021**, *290*, 102365.
- (24) Kim, D. Y.; Shin, W. S. Functional Improvements in Bovine Serum Albumin-Fucoidan Conjugate Through the Maillard Reaction. *Food Chem.* **2016**, *190*, 974–981.
- (25) Bamberger, D.; Hobernik, D.; Konhäuser, M.; Bros, M.; Wich, P. R. Surface Modification of Polysaccharide-Based Nanoparticles with Peg and Dextran and the Effects on Immune Cell Binding and Stimulatory Characteristics. *Mol. Pharmaceutics* **2017**, *14*, 4403–4416.
- (26) Kim, M. H.; Kim, B.; Lim, E. K.; Choi, Y.; Choi, J.; Kim, E.; Jang, E.; Park, H. S.; Suh, J. S.; Huh, Y. M.; Haam, S. Magnetic Nanoclusters Engineered by Polymer-Controlled Self-Assembly for the Accurate Diagnosis of Atherosclerotic Plaques Via Magnetic Resonance Imaging. *Macromol. Biosci.* **2014**, *14*, 943–952.
- (27) Zhang, J.-Y.; Liu, X.-X.; Lin, J.-Y.; Bao, X.-Y.; Peng, J.-Q.; Gong, Z.-P.; Luan, X.; Chen, Y. Biomimetic Engineered Nanocarriers Inspired by Viruses for Oral-Drug Delivery. *Int. J. Pharm.* **2022**, *624*, 121979.
- (28) Park, M. R.; Chun, C.; Ahn, S. W.; Ki, M. H.; Cho, C. S.; Song, S. C. Cationic and Thermosensitive Active Ingredient Conjugated Gels for Enhancing Sustained Human Active Ingredient Delivery. *Biomaterials* **2010**, *31*, 1349–1359.
- (29) Xu, G.; Bao, X.; Yao, P. Active Ingredient and Bsa-Dextran Complex Emulsion Improves Oral Bioavailability and Anti-Tumor Efficacy of Active Ingredient. *Drug Delivery* **2020**, *27*, 1360–1368.
- (30) Pelaseyed, T.; Bergström, J. H.; Gustafsson, J. K.; Ermund, A.; Birchenough, G. M.; Schütte, A.; van der Post, S.; Svensson, F.; Rodríguez-Piñeiro, A. M.; Nyström, E. E.; Wising, C.; Johansson, M. E.; Hansson, G. C. The Mucus and Mucins of the Goblet Cells and Enterocytes Provide the First Defense Line of the Gastrointestinal Tract and Interact with the Immune System. *Immunol. Rev.* **2014**, *260*, 8–20.
- (31) Shan, M.; Gentile, M.; Yeiser, J. R.; Walland, A. C.; Bornstein, T. U.; Chen, K.; He, B.; Cassis, L.; Bigas, A.; Cols, M.; Comerma, L.; Huang, B.; Blander, J. M.; Xiong, H.; Mayer, L.; Berin, C.; Augenlicht, L. H.; Velcich, A.; Cerutti, A. Mucus Enhances Gut Homeostasis and Oral Tolerance by Delivering Immunoregulatory Signals. *Science* **2013**, *342*, 447–453.
- (32) Ren, T.; Wang, Q.; Xu, Y.; Cong, L.; Gou, J.; Tao, X.; Zhang, Y.; He, H.; Yin, T.; Zhang, H.; Zhang, Y.; Tang, X. Enhanced Oral Absorption and Anticancer Efficacy of Cabazitaxel by Overcoming Intestinal Mucus and Epithelium Barriers Using Surface Polyethylene Oxide (PEO) Decorated Positively Charged Polymer-Lipid Hybrid Nanoparticles. *J. Controlled Release* **2018**, *269*, 423–438.
- (33) Wang, A.; Yang, T.; Fan, W.; Yang, Y.; Zhu, Q.; Guo, S.; Zhu, C.; Yuan, Y.; Zhang, T.; Gan, Y. Protein Corona Liposomes Achieve Efficient Oral Active Ingredient Delivery by Overcoming Mucus and Epithelial Barriers. *Adv. Healthc. Mater.* **2019**, *8*, e1801123.
- (34) Cui, Y.; Shan, W.; Liu, M.; Wu, L.; Huang, Y. A Strategy for Developing Effective Orally-Delivered Nanoparticles Through Modulation of the Surface "Hydrophilicity/Hydrophobicity Balance". *J. Mater. Chem. B* **2017**, *5*, 1302–1314.
- (35) Long, L.; Lai, M.; Mao, X.; Luo, J.; Yuan, X.; Zhang, L. M.; Ke, Z.; Yang, L.; Deng, D. Y. Investigation of Vitamin B₁₂-Modified Amphiphilic Sodium Alginate Derivatives for Enhancing the Oral Delivery Efficacy of Peptide Drugs. *Int. J. Nanomedicine* **2019**, *14*, 7743–7758.
- (36) Wang, J.; Tan, J.; Luo, J.; Huang, P.; Zhou, W.; Chen, L.; Long, L.; Zhang, L.-M.; Zhu, B.; Yang, L.; Deng, D. Y. B. Enhancement of Scutellarin Oral Delivery Efficacy by Vitamin B₁₂-Modified Amphiphilic Chitosan Derivatives to Treat Type II Diabetes Induced-Retinopathy. *J. Nanobiotechnol.* **2017**, *15*, 18.
- (37) Singh, A.; Yadagiri, G.; Javaid, A.; Sharma, K. K.; Verma, A.; Singh, O. P.; Sundar, S.; Mudavath, S. L. Hijacking the Intrinsic Vitamin B₁₂ Pathway for the Oral Delivery of Nanoparticles, Resulting in Enhanced in Vivo Anti-Leishmanial Activity. *Biomater. Sci.* **2022**, *10*, 5669–5688.
- (38) Zhang, J.; Field, C. J.; Vine, D.; Chen, L. Intestinal Uptake and Transport of Vitamin B₁₂-Loaded Soy Protein Nanoparticles. *Pharm. Res.* **2015**, *32*, 1288–1303.
- (39) Ke, Z.; Guo, H.; Zhu, X.; Jin, Y.; Huang, Y. Efficient Peroral Delivery of Active Ingredient Via Vitamin B₁₂-Modified Trimethyl Chitosan Nanoparticles. *J. Pharm. Pharm. Sci.* **2015**, *18*, 155–170.
- (40) Verma, A. K.; Sharma, S.; Gupta, P.; Singodia, D.; Kansal, S.; Sharma, V.; Mishra, P. R. Vitamin B₁₂ Grafted Layer-by-Layer Liposomes Bearing Hbsag Facilitate Oral Immunization: Effect of Modulated Biomechanical Properties. *Mol. Pharmaceutics* **2016**, *13*, 2531–2542.
- (41) Francis, M. F.; Cristea, M.; Winnik, F. M. Exploiting the Vitamin B₁₂ Pathway to Enhance Oral Drug Delivery Via Polymeric Micelles. *Biomacromolecules* **2005**, *6*, 2462–2467.
- (42) Roth, W.; Mohamadzadeh, M. Vitamin B₁₂ and Gut-Brain Homeostasis in the Pathophysiology of Ischemic Stroke. *EBioMedicine* **2021**, *73*, 103676.
- (43) Liu, Q.; Yin, B.; Yang, T.; Yang, Y.; Shen, Z.; Yao, P.; Li, F. A General Strategy for Biocompatible, High-Effective Upconversion Nanocapsules Based on Triplet-Triplet Annihilation. *J. Am. Chem. Soc.* **2013**, *135*, 5029–5037.
- (44) Boye, J. I.; Alli, I.; Ismail, A. A. Interactions Involved in the Gelation of Bovine Serum Albumin. *J. Agric. Food Chem.* **1996**, *44*, 996–1004.
- (45) Li, M.; McClements, D. J.; Liu, X.; Liu, F. Design Principles of Oil-in-Water Emulsions with Functionalized Interfaces: Mixed, Multilayer, and Covalent Complex Structures. *Compr. Rev. Food Sci. Food Saf.* **2020**, *19*, 3159–3190.
- (46) Čurlej, J.; Zajác, P.; Čapla, J.; Golian, J.; Benešová, L.; Partika, A.; Fehér, A.; Jakabová, S. The Effect of Heat Treatment on Cow's Milk Protein Profiles. *Foods* **2022**, *11*, 1023.
- (47) Kuan, Y. H.; Bhat, R.; Karim, A. A. Emulsifying and Foaming Properties of Ultraviolet-Irradiated Egg White Protein and Sodium Caseinate. *J. Agric. Food Chem.* **2011**, *59*, 4111–4118.
- (48) Manzocco, L.; Plazzotta, S.; Calligaris, S. Natural Monoterpenes As Potential Therapeutic Agents Against Atherosclerosis. *Foods* **2021**, *10*, 26.
- (49) Celli, G. B.; Liu, Y.; Dadmohammadi, Y.; Tiwari, R.; Raghupathi, K.; Mutilangi, W.; Abbaspourrad, A. Instantaneous Interaction of Mucin with Pectin- and Carrageenan-Coated Nanoemulsions. *Food Chem.* **2020**, *309*, 125795.
- (50) Singh, H.; Sarkar, A. Behaviour of Protein-Stabilised Emulsions under Various Physiological Conditions. *Adv. Colloid Interface Sci.* **2011**, *165*, 47–57.3

(51) Malaki Nik, A.; Wright, A. J.; Corredig, M. Interfacial Design of Protein-Stabilized Emulsions for Optimal Delivery of Nutrients. *Food Funct.* **2010**, *1*, 141–148.

(52) Kim, B.; Yang, J.; Lee, Y. H.; Kim, M. H.; Heo, D.; Lee, E.; Suh, J. S.; Haam, S.; Huh, Y. M. Compensatory UTE/T2W Imaging of Inflammatory Vascular Wall in Hyperlipidemic Rabbits. *PLoS One* **2015**, *10*, No. e0124572.

(53) Lim, E.-K.; Jang, E.; Kim, B.; Choi, J.; Lee, K.; Suh, J.-S.; Huh, Y.-M.; Haam, S. Dextran-Coated Magnetic Nanoclusters As Highly Sensitive Contrast Agents for Magnetic Resonance Imaging of Inflammatory Macrophages. *J. Mater. Chem.* **2011**, *21*, 12473.

(54) Segers, F. M. E.; Ruder, A. V.; Westra, M. M.; Lammers, T.; Dadfar, S. M.; Roemhild, K.; Lam, T. S.; Kooi, M. E.; Cleutjens, K. B. J. M.; Verheyen, F. K.; Schurink, G. W. H.; Haenen, G. R.; van Berkel, T. J. C.; Bot, I.; Halvorsen, B.; Sluimer, J. C.; Biessen, E. A. L. Magnetic Resonance Imaging Contrast-Enhancement with Superparamagnetic Iron Oxide Nanoparticles Amplifies Macrophage Foam Cell Apoptosis in Human and Murine Atherosclerosis. *Cardiovasc. Res.* **2023**, *118*, 3346–3359.

(55) Ma, X.; Bai, Y.; Liu, K.; Han, Y.; Zhang, J.; Liu, Y.; Hou, X.; Hao, E.; Hou, Y.; Bai, G. Ursolic Acid Inhibits the Cholesterol Biosynthesis and Alleviates High Fat Diet-Induced Hypercholesterolemia Via Irreversible Inhibition of HMGCS1 in Vivo. *Phytomedicine* **2022**, *103*, 154233.

(56) Collins, R.; Reith, C.; Emberson, J.; Armitage, J.; Baigent, C.; Blackwell, L.; Blumenthal, R.; Danesh, J.; Smith, G. D.; DeMets, D.; Evans, S.; Law, M.; MacMahon, S.; Martin, S.; Neal, B.; Poulter, N.; Preiss, D.; Ridker, P.; Roberts, I.; Rodgers, A.; Sandercock, P.; et al. Interpretation of the Evidence for the Efficacy and Safety of Statin Therapy. *Lancet* **2016**, *388*, 2532–2561.

(57) Gotto, A. M., Jr. Risks and Benefits of Continued Aggressive Statin Therapy. *Clin. Cardiol.* **2003**, *26*, 3–12.

(58) Cahyana, Y.; Putri, Y. S. E.; Solihah, D. S.; Lutfi, F. S.; Alqurashi, R. M.; Marta, H. Pickering Emulsions As Vehicles for Bioactive Compounds from Essential Oils. *Molecules* **2022**, *27*, 7872.

(59) Kringel, D. H.; Antunes, M. D.; Klein, B.; Crizel, R. L.; Wagner, R.; de Oliveira, R. P.; Dias, A. R. G.; Zavareze, E. D. R. Production, Characterization, and Stability of Orange or Eucalyptus Essential Oil/B-Cyclodextrin Inclusion Complex. *J. Food Sci.* **2017**, *82*, 2598–2605.

(60) Dousti, M.; Sari, S.; Saffari, M.; Kelidari, H.; Asare-Addo, K.; Nokhodchi, A. Loading Pistacia Atlantica Essential Oil in Solid Lipid Nanoparticles and Its Effect on Apoptosis of Breast Cancer Cell Line MDA-MB-231. *Pharm. Dev. Technol.* **2022**, *27*, 63–71.

(61) Kan, X.; Chen, G.; Zhou, W.; Zeng, X. Application of Protein-Polysaccharide Maillard Conjugates As Emulsifiers: Source, Preparation and Functional Properties. *Food Res. Int.* **2021**, *150*, 110740.